(12) INTERNATIONAL APPLICATION PUBLISHED UNDER THE PATENT COOPERATION TREATY (PCT)

(19) World Intellectual Property Organization
International Bureau

(43) International Publication Date
6 September 2013 (06.09.2013)

WIPO | PCT

(10) International Publication Number
WO 2013/127003 A1

(51) International Patent Classification:
A61B 6/00 (2006.01) *A61B 5/0275* (2006.01)
A61B 5/026 (2006.01) *A61B 6/12* (2006.01)

(21) International Application Number:
PCT/CA2013/000202

(22) International Filing Date:
4 March 2013 (04.03.2013)

(25) Filing Language: English

(26) Publication Language: English

(30) Priority Data:
61/606,346 2 March 2012 (02.03.2012) US

(71) Applicant: **LONDON HEALTH SCIENCES CENTRE RESEARCH INC.** [CA/CA]; 750 Base Line Road, Suite 300, London, Ontario N6C 2R5 (CA).

(72) Inventors: **ELLIOTT, Jonathan Thomas**; 352 Emery Street East, London, Ontario N6C 2E5 (CA). **ST. LAWRENCE, Keith**; 426 St. James Street, London, Ontario N5Y 3N8 (CA). **DIOP, Mamadou**; 1581 Mickleborough Court, London, Ontario N6G 5R6 (CA). **LEE, Ting-Yim**; 18 Ambleside Avenue, London, Ontario N6G 4M4 (CA). **TICHAUER, Kenneth M.**; 70 Gould Road, West Lebanon, New Hampshire 03784 (US).

(74) Agent: **RUSTON, David A .**; Sim & McBurney, 330 University Avenue, 6th Floor, Toronto, Ontario M5G 1R7 (CA).

(81) Designated States *(unless otherwise indicated, for every kind of national protection available)*: AE, AG, AL, AM, AO, AT, AU, AZ, BA, BB, BG, BH, BN, BR, BW, BY, BZ, CA, CH, CL, CN, CO, CR, CU, CZ, DE, DK, DM, DO, DZ, EC, EE, EG, ES, FI, GB, GD, GE, GH, GM, GT, HN, HR, HU, ID, IL, IN, IS, JP, KE, KG, KM, KN, KP, KR, KZ, LA, LC, LK, LR, LS, LT, LU, LY, MA, MD, ME, MG, MK, MN, MW, MX, MY, MZ, NA, NG, NI, NO, NZ, OM, PA, PE, PG, PH, PL, PT, QA, RO, RS, RU, RW, SC, SD, SE, SG, SK, SL, SM, ST, SV, SY, TH, TJ, TM, TN, TR, TT, TZ, UA, UG, US, UZ, VC, VN, ZA, ZM, ZW.

(84) Designated States *(unless otherwise indicated, for every kind of regional protection available)*: ARIPO (BW, GH, GM, KE, LR, LS, MW, MZ, NA, RW, SD, SL, SZ, TZ, UG, ZM, ZW), Eurasian (AM, AZ, BY, KG, KZ, RU, TJ, TM), European (AL, AT, BE, BG, CH, CY, CZ, DE, DK, EE, ES, FI, FR, GB, GR, HR, HU, IE, IS, IT, LT, LU, LV, MC, MK, MT, NL, NO, PL, PT, RO, RS, SE, SI, SK, SM, TR), OAPI (BF, BJ, CF, CG, CI, CM, GA, GN, GQ, GW, ML, MR, NE, SN, TD, TG).

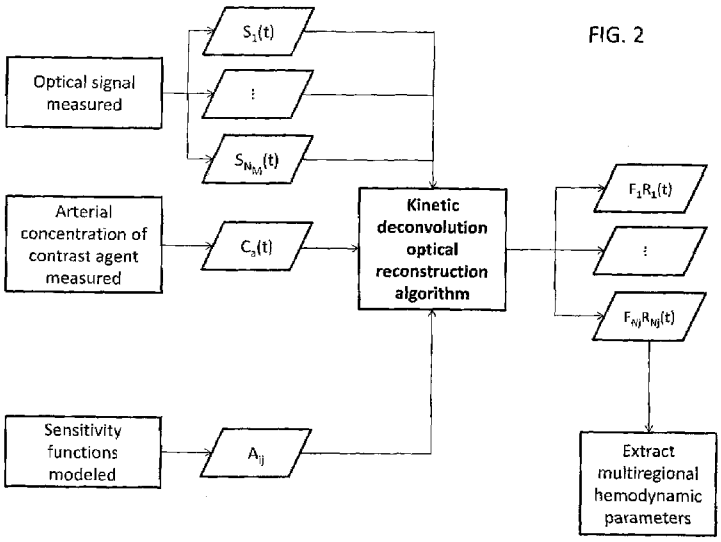
Published:

— *with international search report (Art. 21(3))*

— *before the expiration of the time limit for amending the claims and to be republished in the event of receipt of amendments (Rule 48.2(h))*

(54) Title: KINETIC DECONVOLUTION OPTICAL RECONSTRUCTION METHOD

FIG. 2



(57) Abstract: A method of determining dynamic parameters for a plurality of sub- regions within an interrogation region comprises processing optical image data and measurements of a concentration of contrast agent entering each of the sub-regions to determine a flow-scaled impulse residue function for each of the sub-regions, and calculating dynamic parameters for each sub-region from a respective flow-scaled impulse residue function.

WO 2013/127003 A1

KINETIC DECONVOLUTION OPTICAL RECONSTRUCTION METHOD

Cross-Reference to Related Application

[0001] This application claims the benefit of U.S. Provisional Application No. 61/606,346 to Elliot et al. filed on March 2, 2012, the entire disclosure of which is incorporated herein by reference.

Field of the Invention

[0002] The present invention relates to imaging and in particular, to optical imaging.

Background of the Invention

[0003] Dynamic contrast-enhanced (DCE) techniques are used in biomedical optics to measure tissue dynamic parameters such as for example blood flow (F), blood volume (BV), and mean transit time (MTT) [1]. Analogous to DCE methods for computed tomography (CT) and magnetic resonance (MR) imaging, the methodology requires injecting a contrast agent (CA) into the subject, recording the time-dependent signal change, and applying non-parametric modeling to extract the dynamic parameters.

[0004] If the region being interrogated is considered homogeneous, such as measuring cerebral hemodynamics in a newborn by near-infrared spectroscopy (NIRS) [1], then converting the optical signal into DCE data is straightforward. However, if the region being interrogated is heterogeneous such as an adult head or tomographic imaging of small animals, converting the optical signal into DCE data requires a two-step (TS) method. As in CT and MR imaging, the TS method involves reconstructing a time series of DCE images to determine the change in contrast agent in each image sub-region, followed by applying nonparametric modeling such as deconvolution to the obtained concentration curve of each image sub-region to determine dynamic parameters thereof [2]. For example, DCE data from the adult brain could be isolated using moment analysis of time-resolved NIRS [3]. In another application, a series of DCE fluorescence molecular tomography (FMT) concentration maps are used to obtain dynamic information about a region of interest (ROI) [4]. Unlike CT or MR imaging, extracting dynamic parameters from optical measurements is ill-posed [5].

[0005] The first step of the TS method, namely reconstructing the optical image data to produce a time series of DCE images representing the change in contrast agent in each imaged sub-region, is mathematically ill-posed due to the uncertainty of a sensitivity function, A as the sensitivity function A is a representation of the probability of a photon interacting with a particular imaged sub-region. Thus, there are many potential solutions when determining the change in contrast agent in each imaged sub-region. With the addition of random system noise, it is difficult to differentiate between the potential solutions.

[0006] Improvements in optical image data processing are generally desired. It is therefore an object at least to provide a novel method and apparatus for processing optical image data to determine dynamic parameters.

Summary of the Invention

[0007] Accordingly, in one aspect there is provided a method of determining dynamic parameters for a plurality of sub-regions within an interrogation region, the method comprising processing optical image data and measurements of a concentration of contrast agent entering each of the sub-regions to determine a flow-scaled impulse residue function for each of the sub-regions, and calculating dynamic parameters for each sub-region from a respective flow-scaled impulse residue function.

[0008] In an embodiment, the optical image data is captured upon injection of a contrast agent. The optical image data comprises generating at least one of an equality constraint and an inequality constraint. The at least one equality constraint comprises at least one of assuming the flow-scaled impulse residue function is equal to zero prior to any portion of the contrast agent reaching a respective sub-region, and assuming the flow-scaled impulse residue function is equal to one prior to any portion of the contrast agent exiting the respective sub-region. The at least one inequality constraint comprises assuming that the flow-scaled impulse residue function will decrease after any portion of the contrast agent exits the respective sub-region.

[0009] In an embodiment the dynamic parameters comprise at least one of blood flow, blood volume and mean transit time.

[0010] In an embodiment the contrast agent is a targeted tracer. The dynamic parameters comprise kinetic parameters. The kinetic parameters comprise at least one of

a rate constant governing the extraction of the targeted tracer into an interstitial space, vascular leakage kinetics and binding kinetics.

[0011] According to another aspect there is provided a non-transitory computer readable medium embodying a computer program for execution by a computer to determine dynamic parameters for a plurality of sub-regions within an interrogation region, the computer program comprising program code for processing optical image data and measured concentrations of a contrast agent entering each of the sub-regions to determine a flow-scaled impulse residue function for each of the sub-regions, and program code for calculating dynamic parameters for each sub-region from a respective flow-scaled impulse residue function.

[0012] According to yet another aspect there is provided an apparatus for determining dynamic parameters for a plurality of sub-regions within an interrogation region comprising memory embodying computer program code, and processing structure, the processing structure communicating with the memory, the computer program code when executed by the processing structure causing the apparatus at least to process optical image data and measurements of a concentration of contrast agent entering each of the sub-regions to determine a flow-scaled impulse residue function for each sub-region, and calculate dynamic parameters for each sub-region from a respective flow-scaled impulse residue function.

Brief Description of the Drawings

[0013] Embodiments will now be described more fully with reference to the accompanying drawings in which:

[0014] Figure 1 shows an exemplary construction of a time-density curve as a convolution between the concentration of contrast agent entering an interrogation region and a flow-scaled impulse residue function;

[0015] Figure 2 is a flowchart showing input and output values of a kinetic deconvolution optical reconstruction (KDOR) method;

[0016] Figures 3A to 3D show a comparison of processing an image of a three-layer medium obtained via optical tomography using TS and KDOR methods;

[0017] Figures 4A to 4D show a comparison of processing an image of a cylindrical medium obtained via optical tomography using TS and KDOR methods;

[0018] Figures 5A and 5B show brain specific absorption curves obtained using the KDOR and TS methods, respectively;

[0019] Figures 6A and 6B show average *FR(t)* curves recovered with the KDOR method for extracerebral layer (ECL) and brain tissue, respectively;

[0020] Figures 6C and 6D show average *FR(t)* curves recovered with the TS method for ECL and brain tissue, respectively;

[0021] Figures 7A, 7B and 7C are box-and-whisker plots of blood flow, blood volume and mean transit time for ECL;

[0022] Figures 7D, 7E and 7F are box-and-whisker plots of blood flow, blood volume and mean transit time for brain tissue;

[0023] Figures 8A and 8B show attenuation curves and variance curves, respectively, at baseline, hypocapnia and ischemia conditions;

[0024] Figures 9A and 9B show the recovered flow-scaled impulse residue functions and the recovered brain tissue concentration curves, respectively;

[0025] Figure 10 shows a graph of DCE NIR CBF vs. CT perfusion;

[0026] Figure 11A is a schematic view of a fan-beam system;

[0027] Figure 11B is a perspective view of an optical digimouse;

[0028] Figures 12A and 12B show the mean KDOR-recovered $K_1R(t)$ function for the targeted and untargeted tracers, respectively;

[0029] Figures 12C and 12D show the mean uptake curves recovered with the TS method for the targeted and untargeted tracers, respectively;

[0030] Figures 13A, 13B and 13C are box-and-whisker plots of the kinetic parameters K_1, k2 and the binding potential BP recovered with the KDOR method and the TS method for the background region of the digimouse of Figure 11B; and

[0031] Figures 13D, 13E and 13F are box-and-whisker plots of the kinetic parameters K_1, k2 and the binding potential BP recovered with the KDOR method and the TS method for the tumor region of the digimouse of Figure 11B.

Detailed Description of the Embodiments

[0032] A method for processing optical image data obtained via optical instrumentation to recover dynamic parameters of a plurality of sub-regions is described, and is generally referred to as a kinetic deconvolution optical reconstruction (KDOR) method. The KDOR method comprises processing optical image data and measurements of a concentration of contrast agent entering an interrogation region to determine a flow-scaled impulse residue function for each of the sub-regions, and calculating dynamic parameters for each sub-region from a respective flow-scaled impulse residue function.

[0033] The contrast agent is injected into a subject to enhance the imaging of the specific interrogation region of interest. For example, the interrogation region may be biological tissue. Upon injection of the contrast agent, one or more optical sources are used to direct photons at the interrogation region. The photons pass through the interrogation region and are received by one or more optical detectors positioned at one or more positions around the interrogation region. The received photons are converted to an electrical signal by the optical detectors. The electrical signals are stored as optical image data in memory of a general purpose computing device for processing. As will be appreciated, techniques such as optical tomography or multi-distance diffuse reflectance may be used. Simultaneously, the arterial concentration of the contrast agent delivered to the interrogation region is measured using a dye densitometer or similar device. The optical imaging domain is divided into a number of sub-regions wherein the optical image data is processed via the KDOR method to determine the dynamic parameters of each sub-region. The KDOR method involves the formulation of the separate aspects of spatial or image reconstruction and of kinetic deconvolution into one mathematical expression.

[0034] Spatial or image reconstruction of optical image data following the introduction of a contrast agent into an interrogation region relates a change in an interrogation sub-region optical property caused by the contrast agent to the effect this change has on a measured optical signal. Mathematically, this is represented as:

$$\Delta S_i = \sum_{J=1}^{N_J} A_{i,j}[\mu_j] \cdot \Delta C_j \qquad (1)$$

where ΔC_j is the change in contrast agent concentration in the j^{th} sub-region (which refers to either a layer in surface reflectance measurements or an imaging voxel in tomographic measurements), ΔS_i is the measured change in optical signal at the i^{th} source-detector position, and the sensitivity function, $A_{i,j}$, is the transformation between the change in contrast agent concentration ΔC_j and the measured change in optical signal ΔS_i and is estimated using known diffusion approximation or from Monte Carlo simulations based on an assumed set of interrogation region optical properties μ_j.

[0035] Spatial or image reconstruction is equivalent to solving the inverse problem in Equation 1 through the use of linear or non-linear solvers. The ability to accurately reconstruct the contrast agent concentration C_j depends on the amount of information and type of information contained in the measured change in optical signal ΔS_i and how it is related to the change in contrast agent concentration ΔC_j via the sensitivity function A_{ij}.

[0036] As is well known, optical signals are acquired across one or more dimensions. They may be acquired spatially, through the use of multiple source-detector positions; spectrally, by employing multiple wavelengths of light; or micro-temporally, through the use of photon-counting techniques capable of determining the time-of-flight distribution of detected photons. Each of these types of measurements is used to construct a system of linear operators which can be represented in matrix form:

$$\mathbf{S} = \mathbf{A} \times \mathbf{C} \tag{2a}$$

$$\begin{bmatrix} \Delta S_1 \\ \vdots \\ \Delta S_{N_M} \end{bmatrix} = \begin{bmatrix} A_{1,1} & \cdots & A_{1,N_J} \\ \vdots & \ddots & \vdots \\ A_{N_M,1} & \cdots & A_{N_M,N_J} \end{bmatrix} \times \begin{bmatrix} \Delta C_1 \\ \vdots \\ \Delta C_{N_J} \end{bmatrix} \tag{2b}$$

where $A_{i,j}$ is an element of a Jacobian matrix, which relates the measured optical signal S_i to the change in contrast agent concentration C_j in the j^{th} sub-region. As will be appreciated, the matrix S may include measurements defined for multiple dimensions, and thus may include measurements collected at different time-points, wavelengths, and spatial positions. The matrix S may also be defined for different time-of-flights or different statistical moments, when using photon-counting techniques. The number of unique signals acquired is represented as N_M, and the number of sub-regions in the reconstruction domain is represented as N_J.

[0037] The contrast agent concentration of the j^{th} sub-region C_j measured over a time period is represented as a time-density curve, $C_j(t)$. The time-density curve $C_j(t)$ is represented mathematically as a convolution between the concentration of contrast agent entering an interrogation region, $C_a(t)$, also called the arterial input function (AIF) and a flow-scaled impulse residue function, $F_jR_j(t)$, containing information about the specific dynamic properties of the sub-region such as for example blood flow, blood volume, mean transit time, permeability surface area product, compartmental rate constants, etc. The time-density curve $C_j(t)$ is shown as Equation 3:

$$C_j(t) = F_j \int_0^t C_a(t-u)R_j(u)du \tag{3}$$

[0038] The flow-scaled impulse residue function $F_jR_j(t)$ comprises two components – a scalar F_j representing the blood flow in the interrogation sub-region, multiplied by impulse residue function $R_j(t)$ representing the fraction of contrast agent that remains in the interrogation sub-region at time t. Since impulse residue function $R_j(t)$ is equal to unity at the first appearance of contrast agent, the determination of scalar F_j is readily obtained.

[0039] Figure 1 shows an exemplary construction of time-density curve $C(t)$ 300 as a convolution between the concentration of contrast agent entering an interrogation region $C_a(t)$ 100 and a flow-scaled impulse residue function $FR(t)$ 200.

[0040] The discrete representation of Equation 3 is given by:

$$\mathbf{C} = \mathbf{C_A} \cdot \mathbf{R_F} \tag{4}$$

where $\mathbf{C}$ is a 1 x N_T contrast agent concentration curve, $\mathbf{R_F}$ is a N_A x 1 flow-scaled impulse residue function and $\mathbf{C_A}$ is a N_T x N_A Toeplitz matrix representation of the concentration of contrast agent entering the interrogation region $C_a(t)$ shown as Equation 5:

$$\mathbf{C_A} = \begin{pmatrix} C_{a,t=0} & 0 & 0 & \cdots & 0 \\ C_{a,t=1} & C_{a,t=0} & 0 & \vdots & 0 \\ \vdots & C_{a,t=1} & C_{a,t=0} & \vdots & 0 \\ \vdots & \vdots & \vdots & \ddots & \vdots \\ C_{a,t=N_A-1} & C_{a,t=N_A-2} & C_{a,t=N_A-3} & \cdots & C_{a,t=N_A-N_T} \end{pmatrix} \tag{5}$$

[0041] As will be appreciated, N_T represents the number of time-points in matrix $\mathbf{C}$ and N_A represents the number of time-points in the matrix $\mathbf{C_A}$.

[0042] Theoretically, the N_A x 1 flow-scaled impulse residue function $\mathbf{R_F}$ can be determined by multiplying the inverse (or more generally, the pseudoinverse in the case where $N_A \neq N_T$) of matrix $\mathbf{C_A}$ by matrix $\mathbf{R_F}$ which is determined by minimization of the following problem:

$$\arg\min_{\mathbf{R_F}} \left\{ \left\| \mathbf{C_A} \cdot \mathbf{R_F} - \mathbf{C} \right\|_2^2 \right\} \tag{6}$$

where $\|.\|$ is the Euclidean norm.

[0043] In practice, however, the theoretical approach is susceptible to experimental noise and may result in a highly oscillatory solution for $\mathbf{R_F}$. Thus, regularization or constraints are incorporated when attempting to solve Equation 6, as will now be described.

[0044] Since the flow-scaled impulse residue function *FR(t)* describes a real physiological system, a number of assumptions are incorporated into the constraints that are based on the known behavior of contrast agent introduced into the interrogation region.

[0045] Following the injection of contrast agent into a subject, a finite time is required for the contrast agent to reach the interrogation region from the injection site, the finite time identified as lag time, *L*. Therefore,

$$R(t) = 0, \quad t \leq L \tag{7a}$$

[0046] Once the contrast agent reaches the interrogation region, a minimum amount of time is required before any contrast agent exits the interrogation region—referred to as vascular minimum transit time, *M*. Since the impulse residue function *R(t)* represents the fraction of contrast agent that remains in the interrogation region as a function of time *t* after the injection of the contrast agent, the impulse residue function *R(t)* must be equal to unity during the time in which no contrast agent has left the interrogation region. Therefore,

$$R(t) = 1, \quad L < t \leq L + M \tag{7b}$$

[0047] In mammals, the circulatory system is unidirectional wherein blood enters an organ through one or more arteries, circulates within the organ, and then exits through one or more common veins. Thus, it is assumed that once a contrast agent molecule has left an organ, it will not return back to the organ through a vein, but will only return to the organ through an artery after it is recirculated by the heart. As such,

the impulse residue function $R(t)$ will never increase after the initial appearance of contrast agent. Therefore,

$$\frac{dR(t)}{dt} \leq 0, \quad t > L + M \tag{7c}$$

[0048] The KDOR method is shown generally in Figure 2. As can be seen, an array of measured optical signals, the concentration of contrast agent entering an interrogation region $C_a(t)$ and the sensitivity function, $A_{i,j}$ are used to calculate region-specific flow-scaled impulse residue functions $F_jR_j(t)$. The KDOR method combines Equations 2 and 3 to provide a single step for processing optical image data to recover blood flow parameters of multiple sub-regions within the interrogation region simultaneously. Equation 3 is rewritten as:

$$C_j(t) = F_j \sum_{n}^{t} C_a(n\Delta t) R_j(t - n\Delta t) \tag{8a}$$

where $C_j(t)$ is the region-specific time-dependent contrast agent concentration curve, F_j is region-specific blood flow, Δt is the sampling time interval, and $R_j(t)$ is the region-specific impulse residue function. Equation 8a is represented in matrix form as:

$$\mathbf{C_J} = \mathbf{C_A} \times \mathbf{R_J} \tag{8b}$$

where $\mathbf{R_J}$ is the vector representation of the stacked interrogation region-specific flow-scaled impulse residue functions $FjRj(t)$, and $\mathbf{C_j}$ is the vector representation of the region-specific time-dependent contrast agent concentration curve $C_j(t)$.

[0049] Thus, the combination of Equation 2a and Equation 8b yields:

$$\begin{bmatrix} \Delta S_1 \\ \vdots \\ \Delta S_{N_M \times N_T} \end{bmatrix} = \begin{bmatrix} B_{1,1} & \cdots & B_{1,T_A \times N_J} \\ \vdots & \ddots & \vdots \\ B_{N_M \times N_T,1} & \cdots & B_{N_M \times N_T, N_A \times N_J} \end{bmatrix} \times \begin{bmatrix} F_1 R_1 \\ \vdots \\ F_{N_A \times N_J} R_{N_A \times N_J} \end{bmatrix} \tag{9a}$$

$$\mathbf{S} = \mathbf{B} \times \mathbf{R_F} \tag{9b}$$

where S is a (M_N x T_N) x 1 linearized vector of optical measurements measured at multiple time points, $\mathbf{R_F}$ is a linearized (N_A x N_J) x 1 vector of stacked interrogation region-specific flow-scaled impulse residue functions, $F_jR_j(t)$, and $\mathbf{B}$ is a (N_M x N_T) x (N_A x N_J) compartmentalized matrix comprised from the N_Tx N_A Toeplitz matrix representation of the arterial concentration of contrast agent entering the interrogation

region $C_a(t)$ and the Jacobian matrix A relating the measured optical signal S_i to the change in contrast agent concentration C_j. Matrix **B** is given by:

$$\mathbf{B}=\begin{bmatrix} A_{j=1,i=1}\cdot\mathbf{C}_A & \cdots & A_{j=N_J,i=1}\cdot\mathbf{C}_A \\ \vdots & \ddots & \vdots \\ A_{j=1,i=N_m}\cdot\mathbf{C}_A & \cdots & A_{j=N_J,i=N_m}\cdot\mathbf{C}_A \end{bmatrix} \tag{10}$$

where $\mathbf{C}_A$ is the N_T x N_A triangular matrix described above as Equation 5.

[0050] As mentioned above, a variety of constraints are applied for stability. Generalizing the three constraints shown above as Equations 7a, 7b and 7c to the case where there are N_J regions will now be described.

[0051] There are two types of constraints to be implemented, referred to as equality and inequality constraints represented by matrixes **H** and **G**, respectively. These constraints must satisfy

$$\mathbf{H}\cdot\mathbf{R}_F=0 \tag{11}$$

$$\mathbf{G}\cdot\mathbf{R}_F\geq 0 \tag{12}$$

where matrix $\mathbf{R}_F$ can also be written as:

$$\mathbf{R}_F=\begin{bmatrix}\mathbf{R}_1\\ \mathbf{R}_2\\ \vdots\\ \mathbf{R}_{N_J}\end{bmatrix} \tag{13}$$

and $\mathbf{R}_j$ is the vector representation of the stacked interrogation region-specific flow-scaled impulse residue function $F_jR_j(t)$, where $t = \{t_1, t_1+\Delta t, t_1+2\Delta t, \ldots, t_{N_A}\}$.

[0052] The equality constraints are written in expanded matrix form as:

$$\mathbf{H}=\begin{bmatrix}\mathbf{h}_1 & \tilde{\mathbf{0}} & \cdots & \tilde{\mathbf{0}}\\ \tilde{\mathbf{0}} & \mathbf{h}_2 & \cdots & \tilde{\mathbf{0}}\\ \vdots & \vdots & \cdots & \vdots\\ \tilde{\mathbf{0}} & \tilde{\mathbf{0}} & \cdots & \mathbf{h}_{N_J}\end{bmatrix} \tag{14}$$

where $\mathbf{H}$ is a $[(L_1+M_1-1) + (L_2+M_2-1) + \ldots + (L_j+M_j-1)] \times [N_T \times N_J]$ matrix, $\mathbf{h_j}$ is the compartment of $\mathbf{H}$ containing the constraint that applies only to matrix $\mathbf{R_F}$ of the j^{th} region, and $\tilde{\mathbf{0}}$ is a zero matrix having the dimensions for $\mathbf{H}$ to be properly aligned. Specifically, each zero matrix is dimensioned to have the same number of rows as the compartment row in the $\mathbf{h_j}$ matrix and the same number of columns as the compartment column in the $\mathbf{h_j}$ matrix. The constants L_j and M_j refer to the lag time and minimum transit time of matrix $\mathbf{R_F}$ of the j^{th} region, respectively. The compartment $\mathbf{h_j}$ is represented as:

$$\mathbf{h}_j = \begin{array}{c} \\ L_j \\ \\ \\ \\ M_j-1 \\ \\ \end{array} \overbrace{\begin{bmatrix} 1 & 0 & \cdots & 0 \\ 0 & 1 & \cdots & 0 \\ \vdots & \vdots & \cdots & \vdots \\ 0 & 0 & \cdots & 1 \\ 0 & 0 & \cdots & 0 \\ 0 & 0 & \cdots & 0 \\ \vdots & \vdots & \cdots & \vdots \\ 0 & 0 & \cdots & 0 \end{bmatrix}}^{L_j} \overbrace{\begin{bmatrix} 0 & 0 & 0 & \cdots & 0 & 0 \\ 0 & 0 & 0 & \cdots & 0 & 0 \\ \vdots & \vdots & \vdots & \cdots & \vdots & \vdots \\ 0 & 0 & 0 & \cdots & 0 & 0 \\ 1 & -1 & 0 & \cdots & 0 & 0 \\ 0 & 1 & -1 & \cdots & 0 & 0 \\ \vdots & \vdots & \vdots & \cdots & \vdots & \vdots \\ 0 & 0 & 0 & \cdots & 1 & -1 \end{bmatrix}}^{M_j} \overbrace{\begin{bmatrix} 0 & \cdots & \cdots & 0 \\ 0 & \cdots & \cdots & 0 \\ \vdots & \cdots & \cdots & \vdots \\ 0 & \cdots & \cdots & 0 \\ 0 & \cdots & \cdots & 0 \\ 0 & \cdots & \cdots & 0 \\ \vdots & \cdots & \cdots & \vdots \\ 0 & \cdots & \cdots & 0 \end{bmatrix}}^{N_T-L_j-M} \tag{15}$$

[0053] As can be seen, two non-zero compartments are present in the compartment $\mathbf{h_j}$. The first is an identity matrix and when multiplied with matrix $\mathbf{R_j}$ will satisfy Equation 11 only if the first L_j elements of matrix $\mathbf{R_j}$ are equal to zero. The second compartment of the second row of matrix $\mathbf{h_j}$ is the first difference operator, that is, the discrete equivalent of a first derivative. Multiplied with matrix $\mathbf{R_j}$, Equation 11 will be satisfied in part, only if the elements (L_j+1) to $(L_j + M_j)$ are equal, that is, $\mathbf{R_j}$ is constant for a duration of time equal to the minimum transit time, M_j.

[0054] Similarily, the inequality constraints are written in expanded matrix form as:

$$\mathbf{G} = \begin{bmatrix} \mathbf{g}_1 & \tilde{\mathbf{0}} & \cdots & \tilde{\mathbf{0}} \\ \tilde{\mathbf{0}} & \mathbf{g}_2 & \cdots & \tilde{\mathbf{0}} \\ \vdots & \vdots & \cdots & \vdots \\ \tilde{\mathbf{0}} & \tilde{\mathbf{0}} & \cdots & \mathbf{g}_{N_J} \end{bmatrix} \tag{16}$$

where $\mathbf{G}$ is a $(N_J \times N_T - N_J) \times (N_J \times N_T)$ matrix, $\mathbf{g_j}$ is the compartment of $\mathbf{G}$ containing the constraint that applies only to matrix $\mathbf{R_F}$ of the j^{th} region, and $\tilde{\mathbf{0}}$ is a zero matrix having the dimensions for $\mathbf{G}$ to be properly aligned. Specifically, each zero matrix is

dimensioned to have the same number of rows as the compartment row in the g_j matrix and the same number of columns as the compartment column in the g_j matrix

The compartment g_j is represented as:

$$\mathbf{g}_j = \begin{bmatrix} 1 & 0 & 0 & \cdots & \cdots & \cdots & \cdots & \cdots & \cdots & 0 & 0 & 0 \\ 0 & 1 & 0 & \cdots & \cdots & \cdots & \cdots & \cdots & \cdots & 0 & 0 & 0 \\ 0 & 0 & 1 & \cdots & \cdots & \cdots & \cdots & \cdots & \cdots & 0 & 0 & 0 \\ \vdots & \vdots & \vdots & \ddots & \cdots & \cdots & \cdots & \cdots & \cdots & \vdots & \vdots & \vdots \\ \vdots & \vdots & \vdots & \cdots & \ddots & \cdots & \cdots & \cdots & \cdots & \vdots & \vdots & \vdots \\ \vdots & \vdots & \vdots & \cdots & \cdots & \ddots & \cdots & \cdots & \cdots & \vdots & \vdots & \vdots \\ \vdots & \vdots & \vdots & \cdots & \cdots & \cdots & \ddots & \cdots & \cdots & \vdots & \vdots & \vdots \\ \vdots & \vdots & \vdots & \cdots & \cdots & \cdots & \cdots & \ddots & \cdots & \vdots & \vdots & \vdots \\ \vdots & \vdots & \vdots & \cdots & \cdots & \cdots & \cdots & \cdots & \ddots & \vdots & \vdots & \vdots \\ 0 & 0 & 0 & \cdots & \cdots & \cdots & \cdots & \cdots & \cdots & 1 & 0 & 0 \\ 0 & 0 & 0 & \cdots & \cdots & \cdots & \cdots & \cdots & \cdots & 0 & 1 & 0 \\ 0 & 0 & 0 & \cdots & \cdots & \cdots & \cdots & \cdots & \cdots & 0 & 0 & 1 \\ \hline 0 & 0 & 0 & \cdots & 0 & 0 & 1 & -1 & 0 & \cdots & 0 & 0 \\ 0 & 0 & 0 & \cdots & 0 & 0 & 0 & 1 & -1 & \cdots & 0 & 0 \\ \vdots & \vdots & \vdots & \cdots & \vdots & \vdots & \vdots & \vdots & \vdots & \cdots & \vdots & \vdots \\ \underbrace{0 \quad 0 \quad 0 \quad \cdots \quad 0 \quad 0}_{M_j+L_j-1} & & & & & & \underbrace{0 \quad 0 \quad 0 \quad \cdots \quad 1 \quad -1}_{N_T-M_j-L_j+1} & & & & & \end{bmatrix} \quad (17)$$

[0055] The first row of matrix g_j is an identity matrix of size N_T x N_T. This constrains **Rj** to positive values. The first difference operator appears again in matrix g_j, as the last compartment of the last row. In this case, elements $(Mj + Lj - 1)$ to (N_T) of matrix $\mathbf{R}_j$ must have the property of negative monotonicity, that is, each successive element must not be greater than the previous element. As will be appreciated, this satisfies the constraint described above in Equation 7c.

[0056] Once the constraints represented by Equations 14 and 16 are constructed, matrix $\mathbf{R}_F$, which contains flow-scaled impulse residue functions $FR(t)$ for each sub-region, is solved with a linear solver, by the minimization:

$$\arg\min_{R_F} \left\{ \left\| \mathbf{B} \cdot \mathbf{R}_F - \mathbf{S} \right\|_2^2 \right\}, \quad \text{subject to:} \quad \begin{matrix} \mathbf{H} \cdot \mathbf{R}_F = 0 \\ \mathbf{G} \cdot \mathbf{R}_F = 0 \end{matrix} \quad (18)$$

where matrix $\mathbf{R}_F$ is the combination of stacked vectors $\{\mathbf{R}_1, \mathbf{R}_2, \ldots \mathbf{R}_{NJ}\}$, or the equivalent functions $\{F_1R_1(t), F_2R_2(t), \ldots F_{NJ}R_{NJ}(t)\}$. Thus, the blood flow of each sub-region, $\{F_1, F_2, \ldots F_{NJ}\}$ is recovered.

[0057] Further, integrating over $FjRj(t)$:

$$BV_j = \int_0^{NT} F_j R_j(t) dt \tag{19}$$

yields the blood volume, BV, of the j^{th} region, in an example where the contrast agent is confined to the intravascular space. From the central volume principle, the mean transit time MTT of the j^{th} region is calculated as BV_j / F_j [6].

[0058] A variety of models may be applied to the recovered $F_jR_j(t)$ function, to extract additional information about the kinetic behavior, depending on the application. For example, the surface-area permeability constant of the contrast agent in the j^{th} interrogation region may be extracted by fitting $R_j(t)$ with the adiabatic approximation to a tissue homogeneity (ATH) model:

$$R_j(t) = \begin{cases} 0 & t < L_j \\ 1 & L_j \le t < L_j + M_j \\ E \cdot e^{-\frac{EF}{V_e}(t - M_j)} & t \ge L_j + M_j \end{cases} \tag{20}$$

where M_j is the vascular minimum transit time, F is the blood flow, V_e is distribution volume of tracer in tissue, $E = 1 - e^{-PS/F}$ and represents the fraction of contrast agent that diffuses into tissue during a single pass, and PS is the permeability-surface area product.

[0059] As will be appreciated, the ATH model is only one of many models that may be used to extract additional information from matrix $\mathbf{R_j}$. For example, while the ATH model describes the behavior of a passive contrast agent, a targeted tracer could be used in conjunction with the KDOR method and an appropriate kinetic model to determine additional parameters related to the binding of a targeted receptor in cancer cells [8].

[0060] As will be appreciated, any type of contrast agent may be identified in the above-described method such as for example indocyanine green, Omocyanine (offered by Bayer Schering Pharma, Berlin, Germany), IRDye 800CW Carboxylate (LI-COR Biosciences, Lincoln, Nebraska, USA). Further, targeted contrast agents may be used to measure receptor binding potential. For example, IRDye 800CW EGF may be used to image the epidermal growth factor receptor (LI-COR Biosciences).

[0061] The KDOR method may be used in a number of optical imaging applications. For example, in addition to measuring cerebral hemodynamics, the KDOR method may also be used to assess leakage of contrast agents into brain tissue. Normally the blood-brain barrier is impermeable to contrast agents, however contrast agents such as indocyanine green are able to leak into the brain under certain pathological conditions. As such, the KDOR method may be used to monitor for intra-cerebral hemorrhage following treatment of ischemic stroke by a clot-busting drug (tissue plasminogen activator).

[0062] As another example, in optical tomography involving small-animal models, the KDOR method may be combined with targeted contrast agents. In this example, a region-specific impulse residue function could be analyzed with a kinetic model to retrieve receptor binding parameters, including the binding potential and the maximum binding concentration. One application would be to quantify the expression of specific receptors in pre-clinical cancer models.

[0063] As another example, optical tomography has been proposed as an imaging method to improve the detection of breast tumors, classify malignancy and characterize treatment response. The use of fluorescent non-targeted contrast agents, including indocyanine green or omnocyanine may be used as a means for enhancing sensitivity. The KDOR method provides a method of converting dynamic optical image data into quantitative measurements of tumor hemodynamics and vascular permeability, which are more sensitive markers of tumor types. Similar to pre-clinical studies, targeted contrast agents may be used to measure receptors that are over-expressed in tumors.

[0064] The above-described methodology may be embodied in a machine, process or article of manufacture using standard programming and/or engineering techniques to produce programming software, firmware, hardware or any combination thereof.

[0065] Any resulting program(s), having computer-readable instructions, may be stored within one or more non-transitory computer-usable media such as memory devices or transmitting devices, thereby to yield a computer program product or article of manufacture. As such, functionality may be imparted on a physical device as a

computer program existent as instructions on any computer-readable medium such as on any memory device or in any transmitting device, that are to be executed by a processor.

[0066] Examples of memory devices include but are not limited to hard disk drives, diskettes, optical disks, magnetic tape, semiconductor memories such as FLASH, RAM, ROM, PROMS, and the like. Examples of networks include, but are not limited to, the Internet, intranets, telephone/modem-based network communication, hard-wired/cabled communication network, cellular communication, radio wave communication, satellite communication, and other stationary or mobile network systems/communication links.

[0067] A machine embodying the above-described methodology may comprise one or more processing systems including, for example, computer processing unit (CPU) or processor, memory/storage devices, communication links, communication/transmitting devices, servers, I/O devices, or any subcomponents or individual parts of one or more processing systems, including software, firmware, hardware, or any combination or subcombination thereof.

[0068] Examples of using the KDOR method will now be described.

Example 1

[0069] In a three-sub-region or three-layer medium, continuous-wave diffuse reflectance measurements were simulated for source-detector positions of 10, 20, 30 and 40 mm, as shown in Figure 3A. Layer-specific sensitivity functions (i.e., mean partial path lengths) for each source-detector pair were simulated using Monte Carlo simulations [2]. The time-dependent tracer concentration was generated by convolving a simulated $C_a(t)$ with layer-specific $FR(t)$ functions generated using a gamma variant model [7]. Input F values of 10, 75 and 45 mL/min/100g and input MTT values of 12, 4, and 4.2 sec were used for layers 1, 2 and 3, respectively. Dynamic changes in μ_a for layers 1 and 2 were determined from the generated $FR(t)$ functions assuming that the contrast agent was indocyanine green (Figure 3C). Gaussian noise levels of 5% were added to the optical signal, $C_a(t)$, and the sensitivity functions before two analytical methods were used to extract $FR(t)$. The recovered values of F, BV, and MTT were compared with input values. The accuracy and precision of the two techniques for layers 2 and 3 are summarized as boxplots shown in Figure 3B and were determined by

repeating the procedure three hundred (300) times. The change in attenuation measured at 1cm and 4cm source-detector distances is shown in Figure 3D. Better precision was observed with the KDOR technique compared to the TS technique. In both deeper tissue layers, there was an approximately five times (5x) improvement in precision. Similarly, there was a three times (3x) and one and a half times (1.5x) improvement in the precision of the MTT and BV estimates, respectively.

Example 2

[0070] Simulations were performed using NIRFAST (Dartmouth College, NH) with fan-beam geometry (five detectors directly across from the source, spaced 22.5° apart) [5]. The contrast agent was chosen to be fluorophore. The cylindrical medium used for Example 2 comprised three hemodynamic regions and is shown in Figure 4A. The source is illustrated as arrow AA and the detectors are illustrated as arrows BB. Fluorescence and transmission signals were simulated for sixteen (16) equally spaced projections, while the concentration of the contrast agent fluorophore was varied. Specifically, input F values of 10, 75 and 45 mL/min/100g were used for sub-regions or layers 1, 2 and 3 (shown in Figures 4B), respectively. In the TS approach, fluorophore concentration maps were reconstructed independently for each time-point using the Levenberg-Marquardt minimization algorithm (the time-averaged input concentration of each pixel was used as an initial guess). Regions-of-interest were the same ones used in the forward model. The ROI-averaged CA concentration curves were then deconvolved to obtain the region-specific impulse residue functions in a single step. Figures 4C and 4D summarize the data and recovered functions using both approaches. Specifically, the top of Figure 4C shows a colour map of normalized fluorescence signals for the 16 source positions measured at the 3 detector positions as a function of time during passage of the contrast agent. The bottom portion of Figure 4C shows a sonogram for a single time point (t = 16 seconds). Figure 4D shows the true $FR(t)$ functions for region 2 and region 3, and the recovered $FR(t)$ functions using the TS and KDOR methods. For all regions, KDOR outperformed TS in recovering $FR(t)$. The largest difference between the two techniques was observed in region 2, as the spatial reconstruction did a poorer job of preserving the features of this small region.

Example 3

[0071] Numerical experiments were conducted to compare the accuracy and precision of the KDOR and TS methods. Hemodynamic input parameters used to generate the forward data were held constant for all iterations. The input parameters were blood flow (BF), blood volume (BV) and mean transit time (MTT). For the extracerebral layer (ECL), BF = 5 mL/min/100g, BV = 1 mL/100g, and MTT = 12s. For the brain , BF = 50 mL/min/100g, BV = 4mL/100g and MTT = 5s. Reconstruction was repeated 100 times on the forward data to compare the precision of the KDOR and TS methods.

[0072] Brain specific absorption curves obtained from the TS and KDOR methods are shown in Figures 5A and 5B. The input curve is shown in Figures 5A and 5B and is identified by reference numeral 500. The change in absorption coefficient recovered with the KDOR method is shown in Figure 5A. The KDOR absorption curve was generated by convolving the recovered *FR(t)* with the original arterial input function. The change in absorption coefficient recovered with the TS method is shown in Figure 5B. The TS absorption curve was recovered in the first step of the procedure, and was then analyzed to recover the hemodynamic function.

[0073] Two differences are identified when comparing the absorption curves for the KDOR method (Figure 5A) and the TS method (Figure 5B). First, the TS absorption curve (Figure 5B) shows approximately a -10% bias in the peak absorption compared to the input curve 500, whereas the KDOR absorption curve (Figure 5A) does not show a discernible bias. In addition, the variability in the TS absorption curve (Figure 5B) is two times greater than the variability in the KDOR absorption curve (Figure 5A) around the absorption peak. This variability increased to five times at other time points.

[0074] Figures 6A and 6B show the average *FR(t)* curves recovered with the KDOR method for the ECL and brain tissue, respectively. The ideal *FR(t)* curve is identified in Figure 6A by reference numeral 610 and in Figure 6B by reference numeral 620. Figures 6C and 6D show the average *FR(t)* curves recovered with the TS method for the ECL and brain tissue, respectively. The ideal *FR(t)* curve is identified in Figure 6C by reference numeral 630 and in Figure 6D by reference numeral 640

[0075] Comparing the average *FR(t)* curves for the ECL for the KDOR method (Figure 6A) and for the TS method (Figure 6C), it can be seen that the average *FR(t)* curves closely resemble the ideal *FR(t)* curves, suggesting that there is sufficient information present in the measured signal pertaining to the ECL to allow direct reconstruction with minimal regularization.

[0076] Comparing the average *FR(t)* curves for the brain tissue for the KDOR method (Figure 6B) and for the TS method (Figure 6D), it can be seen that the average *FR(t)* curve for the TS method did not accurately capture the shape of the top of the ideal *FR(t)* curve, which resulted in an underestimation of BF by 11%. The precision of the average *FR(t)* curves was higher for the scalp region, and higher when using the KDOR method compared to the TS method. These results suggest that any errors caused by execution of the TS method during spatial reconstruction propagate into the kinetic analysis, resulting in increased variability and an underestimation bias.

[0077] The three hemodynamic parameters of interest (BF, BV and MTT) were calculated for the two tissue regions (ECL and brain tissue) from the average *FR(t)* curves shown in Figures 6A to 6D. Box-and-whisker plots of the BF, BV and MTT for ECL are shown in Figures 7A, 7B and 7C, respectively. Box-and-whisker plots of the BF, BV and MTT for brain tissue are shown in Figures 7D, 7E and 7F, respectively. In Figures 7A to 7F, boxes are bound by the 1st and 3rd quartiles, and the median is given by the center line. Error bars are the minimum and maximum, with outliers shown in crosses. The dashed lines show the true value of the parameter.

[0078] As can be seen, the KDOR method was more accurate in recovering the hemodynamic parameters than the TS method. In particular, the mean error in recovered CBF was -1.4% using the KDOR method, compared with -11% using the TS method. The precision of the CBF estimate derived from the KDOR method was approximately two times greater than the precision derived from the TS method.

Example 4

[0079] A Duroc-cross pig was acquired. Following induction with 1.75-3% isoflurane, the pig was tracheotomized and mechanically ventilated on oxygen/medical air. A rubber probe holder was placed on the head and fixed in place with tissue glue, and three surgical incisions were made, one each on the caudial, rostral and lateral sides

of the probe holder, so that only the segment medial to the holder was left intact. This was done to reduce the blood flow in the scalp, which is much higher in the pig due to high vascularization of the thick temporalis muscles originating at the temperoparietal region of the head [9].

[0080] Following the scalp surgery, the animal was given a 1-hour stabilization period before the start of the validation experiment. DCE-NIR and CT perfusion measurements were made for each of three physiological conditions: baseline, hypocapnia, and ischemia. A DCE NIR measurement consisted of collecting multi-channel TR NIR data from the surface of the head during the bolus injection of ICG (0.1 mg/kg, Cardiogreen, Signa-Aldrich, St. Louis, MO), and simultaneously acquiring the Ca(t) by dye densitometry. The CT perfusion measurement was performed following the DCE-NIR measurement. Hypocapnia was achieved by increasing the respiration rate on the ventilator, resulting in the overexpiration of CO_2 and subsequent increase in CBF as a compensatory mechanism. Ischemia was achieved by drilling a burr hole through the scalp and scull just lateral to the probe holder at the half way point, and infusing endothelin-1 (ET-1), a potent vasoconstrictor, directly into the cortical tissue via a 30-Ga needle angled towards the midline. The objective was to cause widespread ischemia across the hemisphere beneath the probe holder.

[0081] A representative example of attenuation curves at baseline, hypocapnia and ischemia conditions is shown in Figure 8A. A representative example of variance curves at baseline, hypocapnia and ischemia conditions is shown in Figure 8B. As can be seen, the attenuation curves exhibit little diference in shape when acquired under the three conditions, with the exception of a slight difference in the washout of dye under hypocapnia. When examining the change in variance curves, there is a significant shape difference between the ischemia curve compared with the baseline and hypocapnia curves. It is noted that under the baseline and hypocapnia conditions, the variance curve contains a significant fast component that arrives earlier than the attenuation signal, which is slow and persistent. This fast component is abolished under the ischemia condition, which affects only the blood flow in the brain tissue. This suggests that the variance curve is maximally sensitive to changes occurring in the brain.

[0082] The KDOR method was used to analyze the entire data set, collected at four distances and defined for the three conditions. The recovered flow-scaled impulse

residue functions *FR(t)* are shown in Figure 9A. As can be seen, there is a difference in height for each of the three conditions. It is noted that the maximum height of the curves shown in Figure 9A is equal to blood flow.

[0083] The recovered brain tissue concentration curves for the three conditions are shown in Figure 9B. It is noted that under the baseline and hypocapnia conditions, the first pass of the dye decreased to about 15% of the maximum before recirculation caused transient fluctuations. The shape of the concentration curves is characteristic of brain dye curves under non-ischemic conditions, confirmed by measurements in piglets [10], directly on the brain of adult pigs [9] and in CT region-of-interest curves. The recovered curve under the ischemia condition shows a reduction in the amount of dye delivered to the brain tissue, and has slightly slower kinetics suggesting that flow was reduced. Quantitative comparisons were made under these three conditions with CT perfusion measurements calculated for appropriate regions-of-interest. These values are summarized in Table 1:

	Baseline		Hypocapnia		Ischemia	
	DCE NIR	CT	DCE NIR	CT	DCE NIR	CT
CBF (ml min^{-1} $100g^{-1}$)	75.0	70.1	61.5	62.9	27.2	38.1
CBV (ml $100g^{-1}$)	3.74	5.38	3.13	4.38	3.33	4.41
MTT (sec)	2.99	4.61	3.06	4.18	7.33	6.93

Table 1: The DCE NIR and CT perfusion recovered hemodynamic values for baseline, hypocapnia and ischemia conditions

[0084] As can be seen in Table 1, for each condition, the DCE NIR and CT measurements are in agreement, however the DCE NIR measurements exhibit slightly smaller blood volumes than CT perfusion.

[0085] Figure 10 shows a graph of DCE NIR CBF vs. CT perfusion. For this graph, twelve (12) measurements were taken from five (5) adult pigs.

Example 5

[0086] The KDOR method was used to characterize the behavior of targeted tracers which bind to receptors of interest. Targeted tracer methods are used in imaging modalities such as positron emission tomography (PET) and planar fluorescence

imaging to quantify molecular expression of epidermal growth factor receptor (EGFR) in tumors [11]. Similar to CT perfusion, PET molecular imaging involves two-steps: spatial reconstruction of tracer concentration and subsequent kinetic analysis. Spatial reconstruction in PET is a known problem: the radioisotope undergoes positive beta decay, and subsequent positron-electron annihilation. Producing two 511 keV gamma photons that are emitted at almost 180° can be used to localize the source of the decay with sub-centimeter resolution. However, using a two-step (TS) process in optical tomography results in loss-of-information that will decrease the accuracy of recovered kinetic parameters. As an alternative approach, the KDOR method was used to characterize the *R(t)* function for each region directly and to obtain information from these recovered functions by fitting them with a kinetic model.

[0087] In molecular imaging with targeted and untargeted probes, the uptake of a tracer by the tissue is described by the following convolution:

$$C(t) = K_1 C_a(t) \times R(t) \tag{21}$$

where K_1 is the rate constant governing the extraction of the tracer into the interstitial space, $C_a(t)$ is the concentration of contrast agent entering an interrogation region, and $R(t)$ is the impulse residue function.

[0088] If an untargeted tracer is selected that has the same concentration of contrast agent entering the interrogation region $C_a(t)$ as the targeted tracer, and the binding kinetics (k_3 and k_4) are faster than the vascular leakage kinetics (k_2), then the following Equations describe the impulse residue function for the targeted $R_t(t)$ and untargeted $R_u(t)$ tracers:

$$R_t(t) = e^{-\frac{k_2}{1+BP}t} \tag{22}$$

$$R_u(t) = e^{-k_2 t} \tag{23}$$

where BP is the binding potential and is equal to k_3/k_4 [11].

[0089] In this example, the KDOR method was used to recover the $K_1R(t)$ function from each region. The kinetic parameters (K_1, k_2, BP) were recovered by optimizing the following Equation:

$$\min_{K_1,k_2,BP}\left\{\left\|K_1 R_{T,rec}(t) - K_1 e^{-\frac{k_2}{1+BP}t}\right\|_2^2 + \left\|K_1 R_{U,rec}(t) - K_1 e^{-k_2 t}\right\|_2^2\right\} \tag{24}$$

[0090] Optimization was performed in MATLAB™ using the *fminsearchbnd* function.

[0091] Numerical simulations were performed with NIRFAST using a heterogenous optical digimouse [12] and a fan-beam FMT system [13]. Figures 11A and 11B show the fan-beam system FMT 700 and the optical digimouse 800 used for the simulations. As can be seen, the fan-beam FMT system 700 comprises a source 710 and five detectors 720. The five detectors 720 rotate around a gantry 730 to collect tomography data. The optical digimouse 800 comprises a head 810 having a tumor region 820 and a background region 830.

[0092] Fluorescence at the targeted (800nm) and untargeted (700nm) dye wavelengths was simulated in the head 810 of the digimouse 800 and the signal was recorded in the five detectors 720 simultaneously with an integration time of 12 seconds. This was repeated for 32 source positions, with a rotation time between positions of 32 seconds. A complete set of optical data (32 source x 5 detectors) was acquired every 23.5 minutes for 2.5 hours.

[0093] Reconstruction of kinetic parameters was performed using the KDOR and TS methods. For the KDOR method, the region-specific $K_1R(t)$ functions for the targeted and untargeted tracers were reconstructed and kinetic parameters were extracted by minimizing Equation 24. For the TS method, a time-series of targeted and untargeted concentration maps were reconstructed using a Levenberg-Marquardt approach [14] with hard anatomical priors. These regions of interest were then used to define the tracer uptake curves. Kinetic parameters were extracted by fitting the tracer uptake curves with the convolution of Equation 21 (above). Reconstruction was performed on a homogeneous mesh ($\mu_a = 0.01$ mm^{-1}, $\mu_s' = 1.0$ mm^{-1}). To compare the precision and accuracy of the two approaches, the reconstruction procedure was repeated 100 times.

[0094] Figures 12A and 12B show the mean KDOR-recovered $K_1R(t)$ function for the 100 repetitions for the targeted and untargeted tracers, respectively. The ideal $K_1R(t)$ function is identified by reference numeral 900 and the mean model-fitted $K_1R(t)$ function is identified by reference numeral 910.

[0095] Figures 12C and 12D show the mean $C(t)$ uptake curves recovered with the TS method for the 100 repetitions for the targeted and untargeted tracers,

respectively. The ideal *C(t)* uptake curve is identified by reference numeral 920 and the mean model-fitted uptake curve is identified by reference numeral 930.

[0096] Comparing Figures 12A and 12B to Figures 12C and 12D, it will be appreciated that the KDOR method shows a strong agreement with the ideal and mean model-fitted $K_1R(t)$ functions. The percent difference in area under the ideal and mean model-fitted $K_1R(t)$ functions was less than 0.01% in all cases. The uptake curve recovered using the TS method show marked deviations from the ideal and mean model-fitted uptake curves.

[0097] Kinetic parameters were recovered by fitting the corresponding dual-tracer model functions to these curves. Box-and-whisker plots of K_1, k2 and the binding potential BP recovered with the KDOR method and the TS method for the background region are shown in Figures 13A, 13B and 13C, respectively. Box-and-whisker plots of K_1, k2 and the binding potential BP recovered with the KDOR method and the TS method for the tumor region are shown in Figures 13D, 13E and 13F, respectively. In Figures 13A to 13F, boxes are bound by the 1st and 3rd quartiles, and the median is given by the center line. Error bars are the minimum and maximum, with outliers shown in crosses. The dashed lines show the true value of the parameter.

[0098] As can be seen in Figures 13A to 13F, the KDOR method is more accurate and precise in recovering the kinetic parameters K_1, k2 and the binding potential BP. The TS method is only capable of accurately recovering the background K1 parameter, and even in this case, the TS method exhibits high variability.

[0099] Although embodiments have been described above with reference to the accompanying drawings, those of skill in the art will appreciate that variations and modifications may be made without departing from the scope thereof as defined by the appended claims.

References

[00100] 1. D. W. Brown, P. A. Picot, J. G. Naeini, R. Springett, D. T. Delpy, and T.Y. Lee. Pediatr. Res. 51 (2002).

[00101] 2. J. T. Elliott, M. Diop, K. M. Tichauer, T. Y. Lee and K. St. Lawrence. J. Biomed. Opt. 15, 3 (2010).

[00102] 3. A. Liebert, H. Wabnitz, J. Steinbrink, H. Obrig, M. Moller, R. Macdonald, A. Villringer and H. Rinneberg. Appl. Opt. 43, 15 (2004).

[00103] 4. X. Liu, D. Wang, F. Liu, and J. Bai. Opt. Express. 18, 6 (2010).

[00104] 5. F. Leblond, K. M. Tichauer, R. W. Holt, F. El-Ghussein, and B. W. Pogue. Opt. Lett. 36, 19 (2011).

[00105] 6. K. L. Zierler. Circ. Res. 16 (1965).

[00106] 7. H. K. Thompson, C. F. Starmer, R. E. Whalen, and H. D. McIntosh. Circ. Res. 14 (1964).

[00107] 8. E. M. Hillman and A. Moore. Nat. Photonics. 1. (2007).

[00108] 9. Elliott, J. T., Milej D., Gerega A., Weigl W., Diop M., Morrison L.B., Lee T-Y., Liebert A., and St. Lawrence K., "Variance of time-of-flight distribution is sensitive to cerebral blood flow as demonstrated by ICG bolus-tracking measurements in adult pigs," Biomed. Opt. Exp. 4(2), 206-218 (2013).

[00109] 10. Brown D.W., Picot P.A., Naeini J.G., Springett, R., Delpy D.T., and Lee T-Y, "Quantitative near infrared spectroscopy measurement of cerebral hemodynamics in newborn piglets," Pediatr. Res. 51, 564-570 (2002).

[00110] 11. Tichauer KM, Samkoe KS, Klubben WS, Hasan T, Pogue BW 2012 "Advantages of a dual-tracer model over reference tissue models for binding potential measurement in tumors," Phys Med Biol 57 6647-6659.

[00111] 12. Dogdas B, Stout D, Chatziioannou A, and Leahy RM 2007 "Digimouse: A 3D Whole Body Mouse Atlas from CT and Cryosection Data," Phys Med Biol 52(3) 577-87.

[00112] 13. Tichauer KM, Samkoe KS, Klubben WS, Hasan T, Pogue BW 2012 "Advantages of a dual-tracer model over reference tissue models for binding potential measurement in tumors," Phys Med Biol 57 6647-6659.

[00113] 14. Dehghani H, Eames ME, Yalavarthy PK, Davis SC, Srinivasan S, Carpenter CM, Pogue BW, Paulsen KD 2008 "Near infrared optical tomography using

NIRFAST: Algorithm for numerical model and image reconstruction," Commun Numer Methods 25(6) 711-32.

What is claimed is:

1. A method of determining dynamic parameters for a plurality of sub-regions within an interrogation region, the method comprising:

processing optical image data and measurements of a concentration of contrast agent entering each of the sub-regions to determine a flow-scaled impulse residue function for each of the sub-regions; and

calculating dynamic parameters for each sub-region from a respective flow-scaled impulse residue function.

2. The method of claim 1 wherein the optical image data is captured upon injection of a contrast agent.

3. The method of claim 1 or 2 wherein processing the optical image data comprises generating at least one of an equality constraint and at least one of an inequality constraint.

4. The method of claim 3 wherein the at least one equality constraint comprises at least one of:

assuming the flow-scaled impulse residue function is equal to zero prior to any portion of the contrast agent reaching a respective sub-region; and

assuming the flow-scaled impulse residue function is equal to one prior to any portion of the contrast agent exiting the respective sub-region.

5. The method of claim 4 wherein the at least one inequality constraint comprises assuming that the flow-scaled impulse residue function will decrease after any portion of the contrast agent exits the respective sub-region.

6. The method of any one of claims 1 to 5 wherein the dynamic parameters comprise at least one of blood flow, blood volume and mean transit time.

7. The method of any one of claims 1 to 5 wherein the contrast agent is a targeted tracer.

8. The method of claim 7 wherein the dynamic parameters comprise kinetic parameters.

9. The method of claim 8 wherein the kinetic parameters comprise at least one of a rate constant governing the extraction of the targeted tracer into an interstitial space, vascular leakage kinetics and binding kinetics.

10. The method of any one of claims 1 to 9 wherein the interrogation region is biological tissue.

11. The method of any one of claims 1 to 10 wherein the calculating comprises solving a matrix comprising each of the flow-scaled impulse residue functions of each of the sub-regions.

12. A non-transitory computer readable medium embodying a computer program for execution by a computer to determine dynamic parameters for a plurality of sub-regions within an interrogation region, the computer program comprising:

program code for processing optical image data and measured concentrations of a contrast agent entering each of the sub-regions to determine a flow-scaled impulse residue function for each of the sub-regions; and

program code for calculating dynamic parameters for each sub-region from a respective flow-scaled impulse residue function.

13. The non-transitory computer readable medium of claim 12 wherein the dynamic parameters comprise at least one of blood flow, blood volume and mean transit time.

14. The non-transitory computer readable medium of claim 12 wherein the contrast agent is a targeted tracer.

15. The non-transitory computer readable medium of claim 14 wherein the dynamic parameters comprises kinetic parameters.

16. The non-transitory computer readable medium of claim 15 wherein the kinetic parameters comprise at least one of a rate constant governing the extraction of the targeted tracer into an interstitial space, vascular leakage kinetics and binding kinetics.

17. An apparatus for determining dynamic parameters for a plurality of sub-regions within an interrogation region comprising:

memory embodying computer program code; and

processing structure, the processing structure communicating with the memory, the computer program code when executed by the processing structure causing the apparatus at least to:

process optical image data and measurements of a concentration of contrast agent entering each of the sub-regions to determine a flow-scaled impulse residue function for each sub-region; and

calculate dynamic parameters for each sub-region from a respective flow-scaled impulse residue function.

18. The apparatus of claim 17 wherein the dynamic parameters comprise at least one of blood flow, blood volume and mean transit time.

19. The apparatus of claim 17 wherein the contrast agent is a targeted tracer.

20. The apparatus of claim 19 wherein the dynamic parameters comprises kinetic parameters.

21. The apparatus of claim 20 wherein the kinetic parameters comprise at least one of a rate constant governing the extraction of the targeted tracer into an interstitial space, vascular leakage kinetics and binding kinetics.

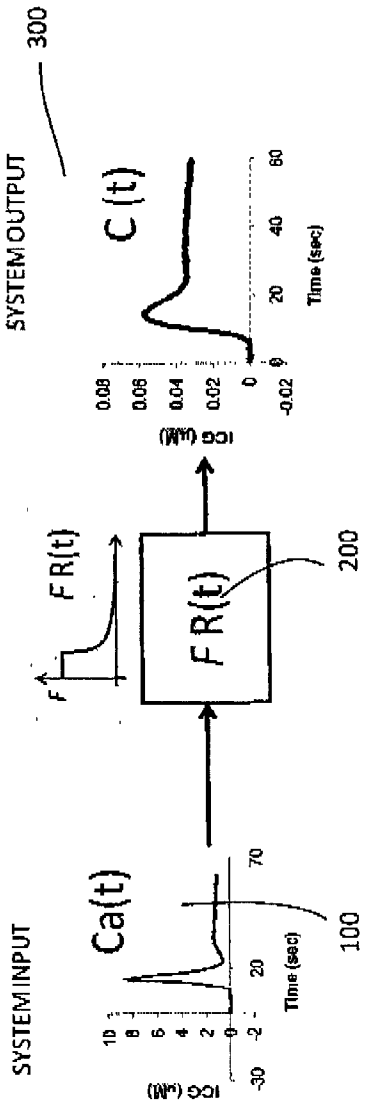

SYSTEM INPUT
Ca(t)
ICG (μM)
Time (sec)
100
F R(t)
F
200
SYSTEM OUTPUT
300
C (t)
ICG (μM)
Time (sec)

FIG. 1

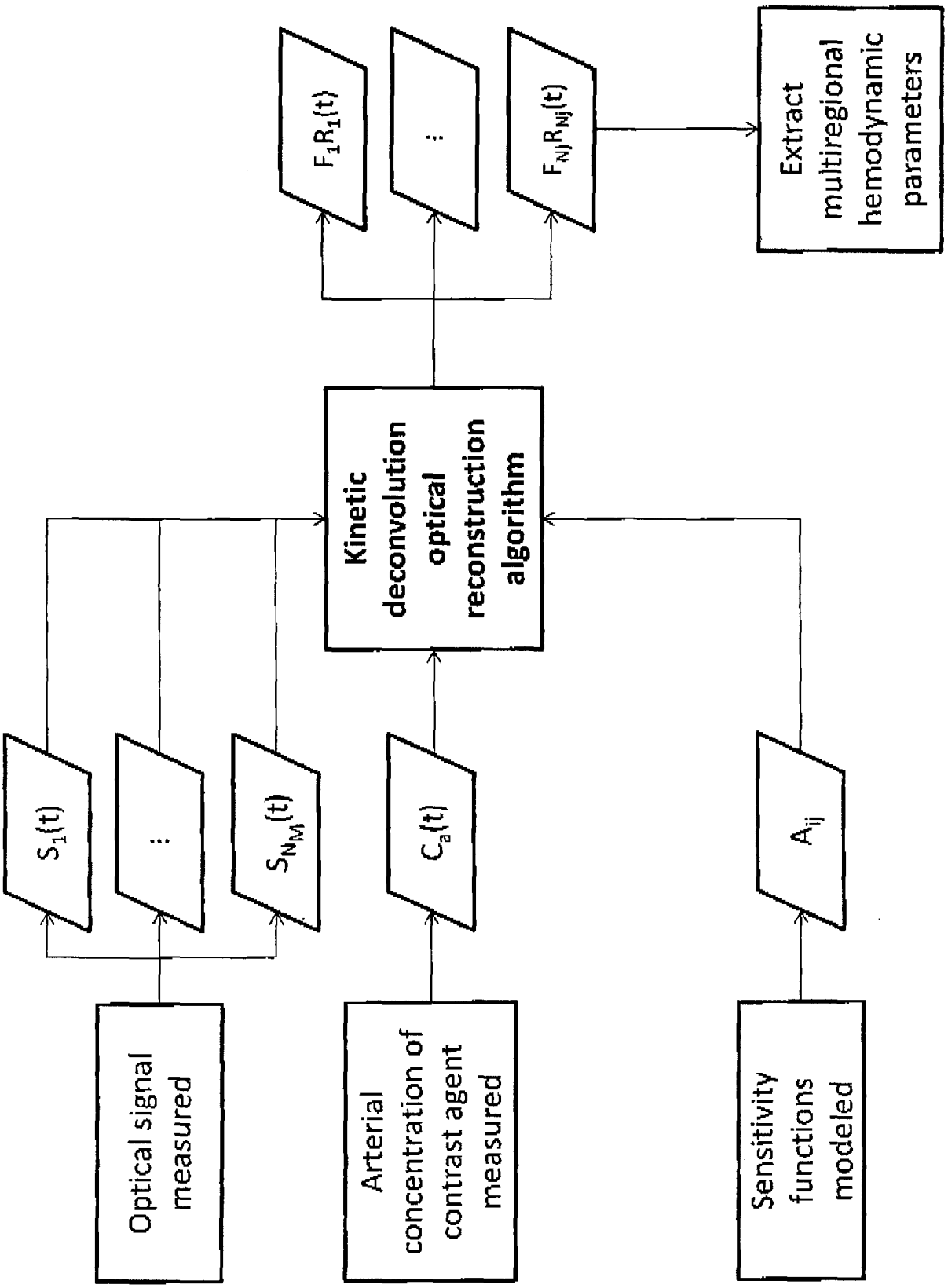

Optical signal measured
Arterial concentration of contrast agent measured
Sensitivity functions modeled
$S_1(t)$
:
$S_{N_M}(t)$
$C_a(t)$
A_{ij}
Kinetic deconvolution optical reconstruction algorithm
$F_1R_1(t)$
:
$F_{Nj}R_{Nj}(t)$
Extract multiregional hemodynamic parameters

FIG. 2

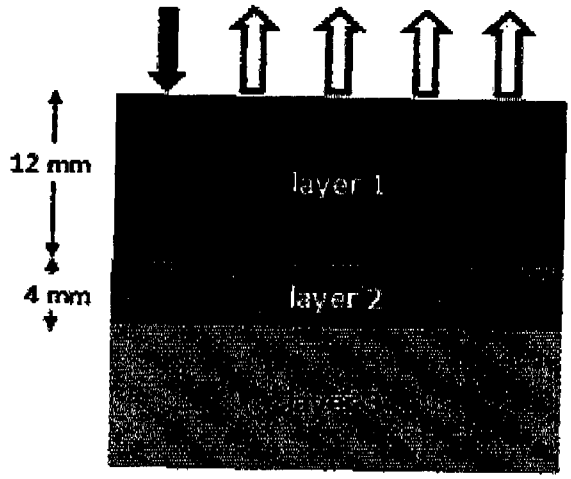

12 mm
4 mm
layer 1
layer 2

FIG. 3A

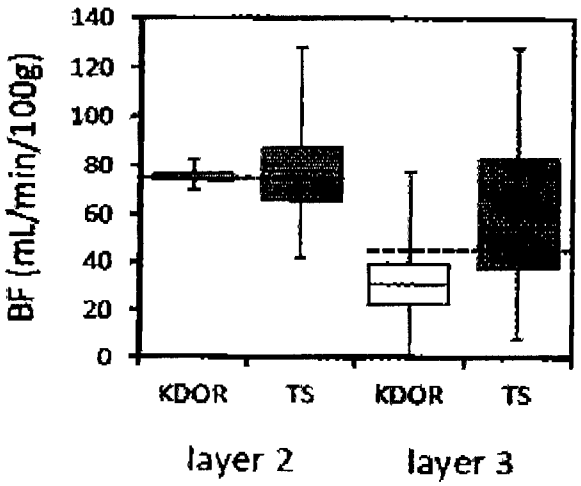

BF (mL/min/100g)
140
120
100
80
60
40
20
0
KDOR
TS
KDOR
TS
layer 2
layer 3

FIG. 3B

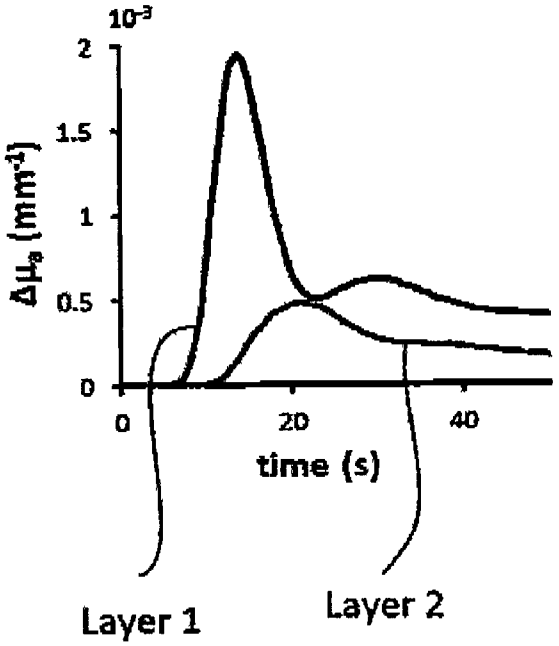

10⁻³
2
1.5
1
0.5
0
Δμa (mm⁻¹)
0
20
40
time (s)
Layer 1
Layer 2

FIG. 3C

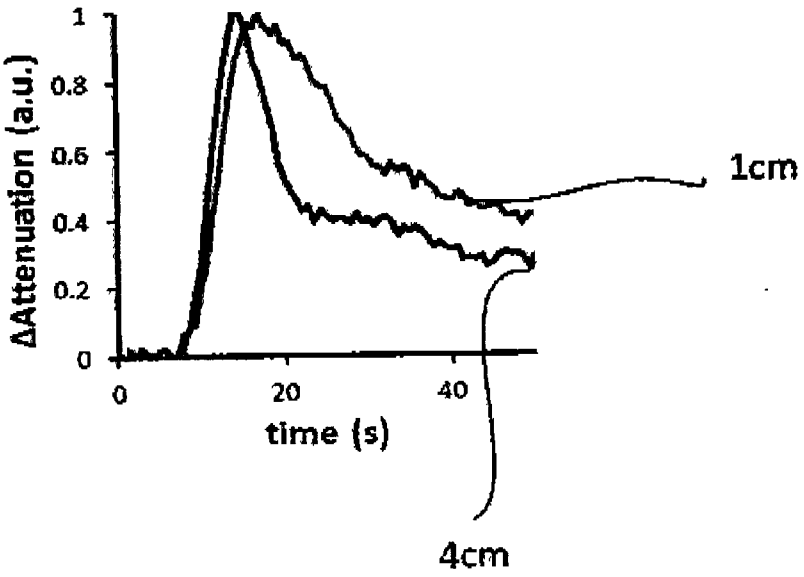

1
0.8
0.6
0.4
0.2
0
ΔAttenuation (a.u.)
0
20
40
time (s)
1cm
4cm

FIG. 3D

FIG. 4A

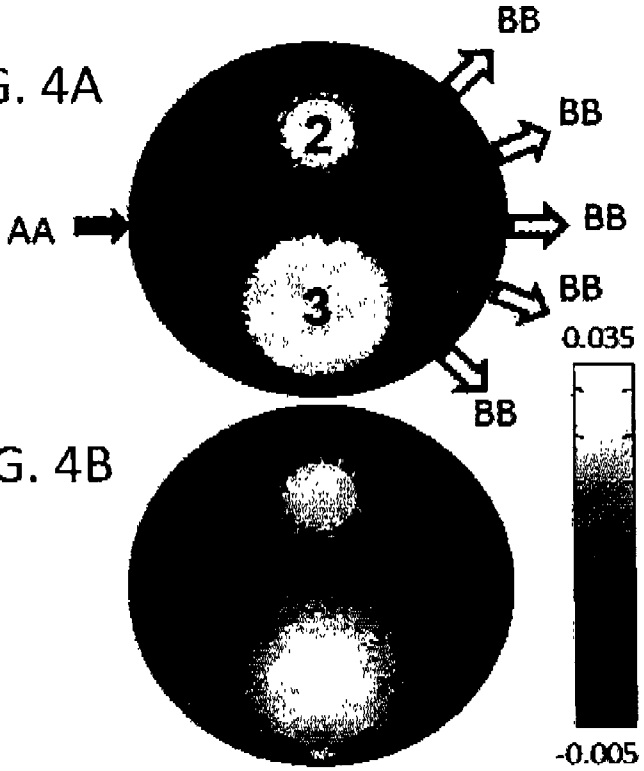


FIG. 4B

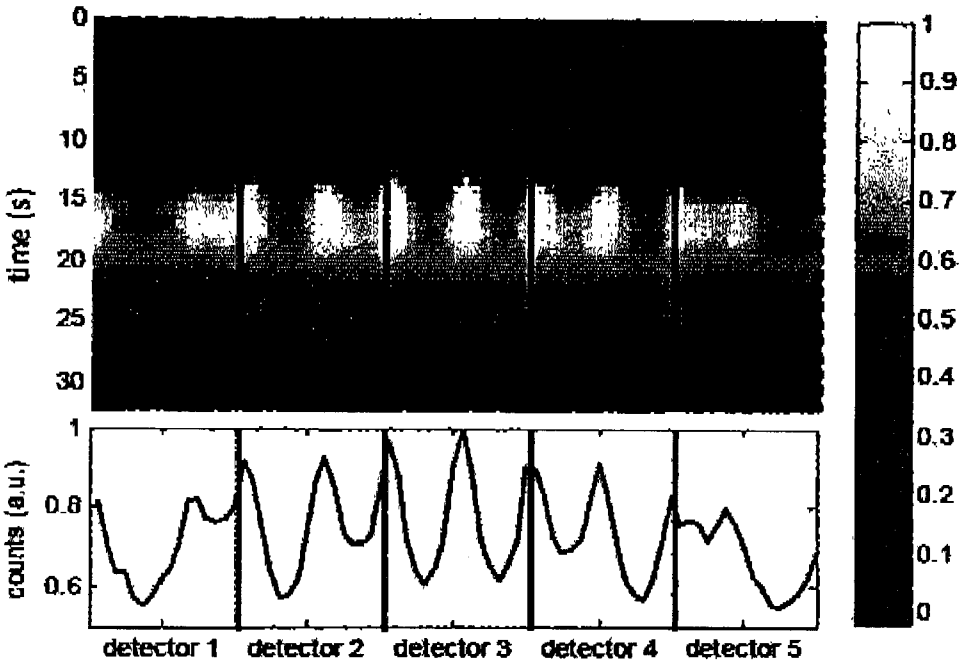

time (s)
0
5
10
15
20
25
30
counts (a.u.)
1
0.8
0.6
detector 1
detector 2
detector 3
detector 4
detector 5
1
0.9
0.8
0.7
0.6
0.5
0.4
0.3
0.2
0.1
0

FIG. 4C

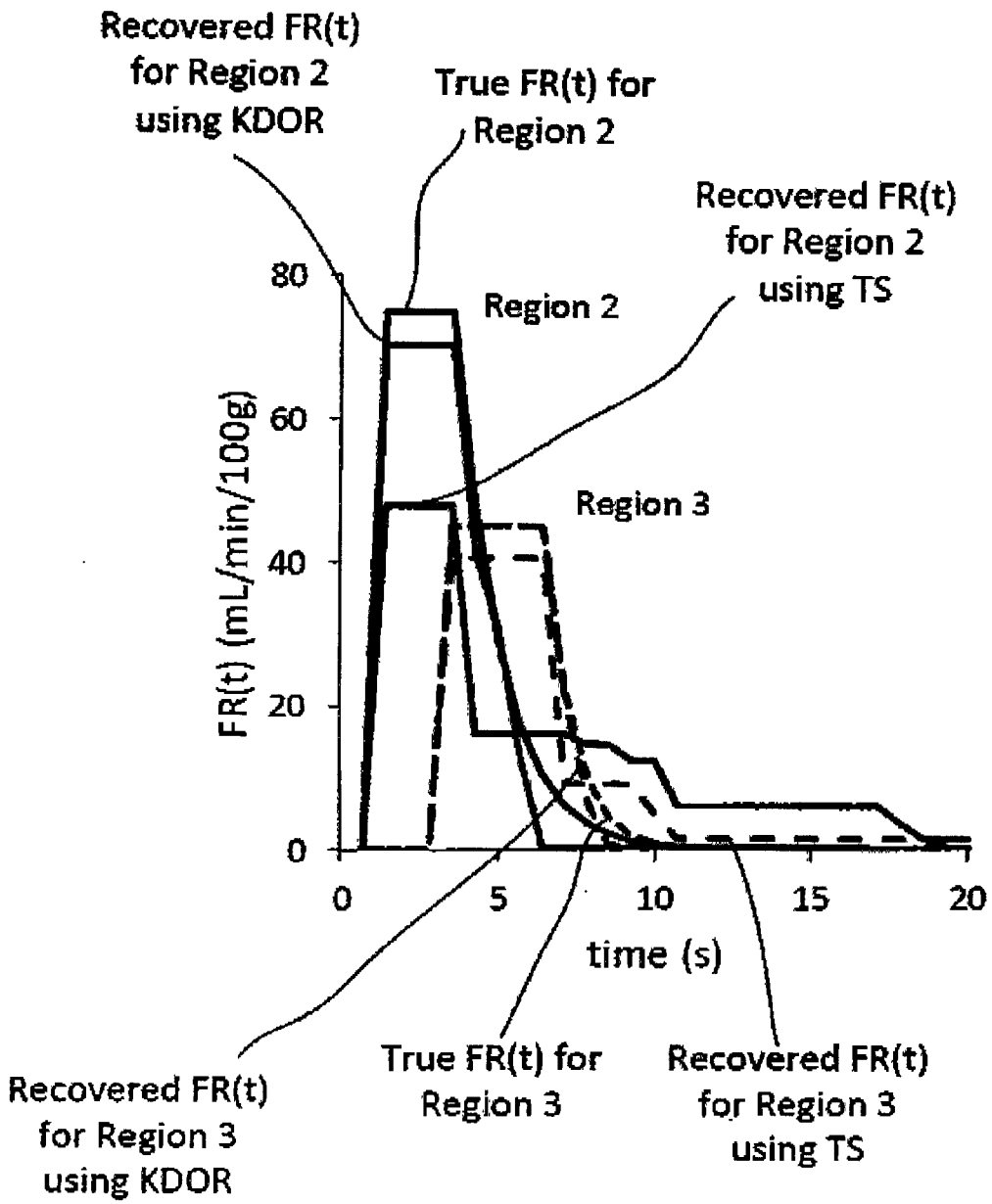

Recovered FR(t) for Region 2 using KDOR
True FR(t) for Region 2
Recovered FR(t) for Region 2 using TS
Region 2
Region 3
FR(t) (mL/min/100g)
80
60
40
20
0
0
5
10
15
20
time (s)
Recovered FR(t) for Region 3 using KDOR
True FR(t) for Region 3
Recovered FR(t) for Region 3 using TS

FIG. 4D

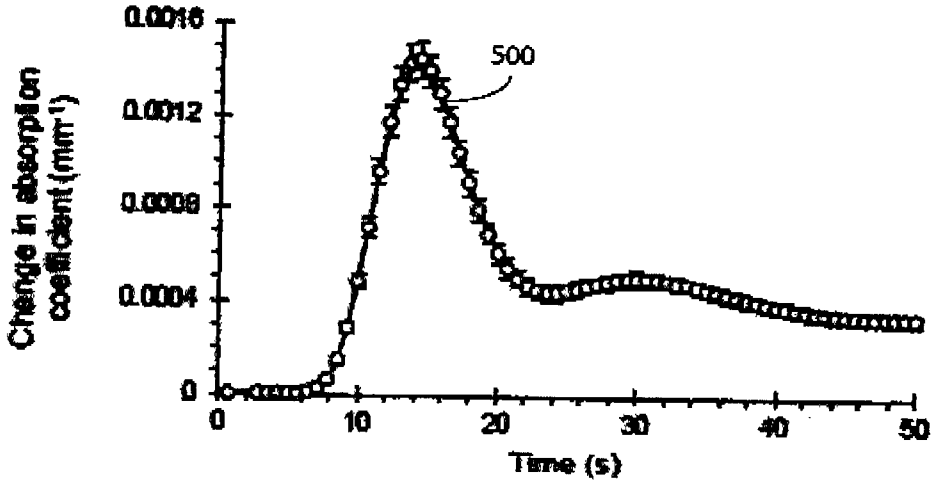

0.0016
0.0012
0.0008
0.0004
0
Change in absorption coefficient (mm⁻¹)
500
0
10
20
30
40
50
Time (s)

FIG. 5A

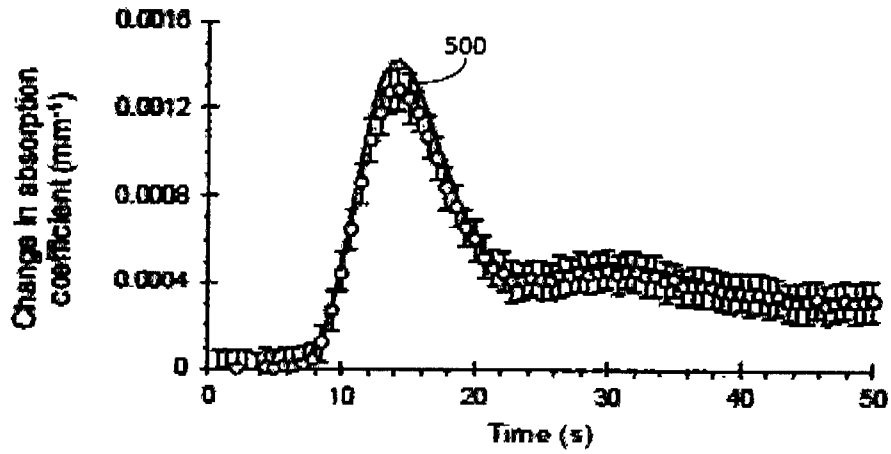

0.0016
0.0012
0.0008
0.0004
0
Change in absorption coefficient (mm⁻¹)
500
0
10
20
30
40
50
Time (s)

FIG. 5B

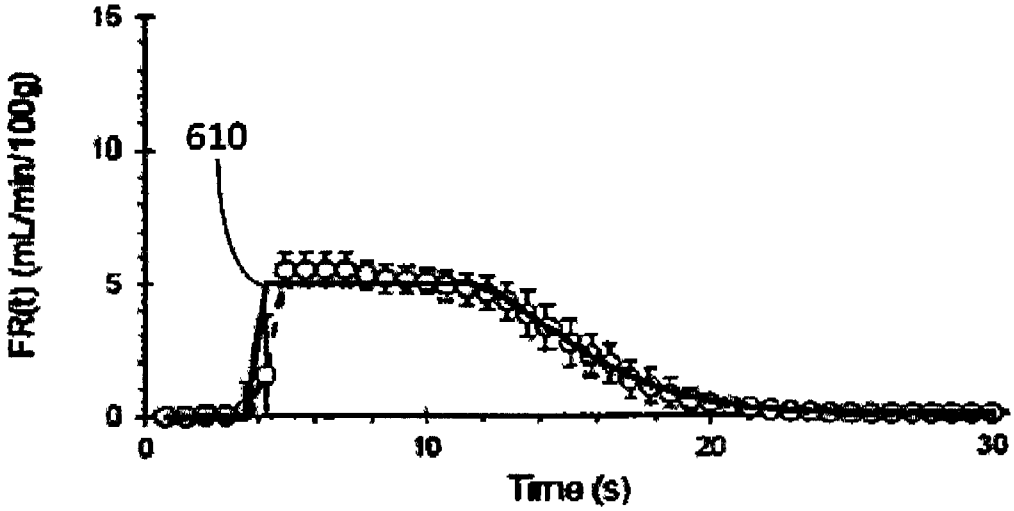

15
10
5
0
FR(t) (mL/min/100g)
610
0
10
20
30
Time (s)

FIG. 6A

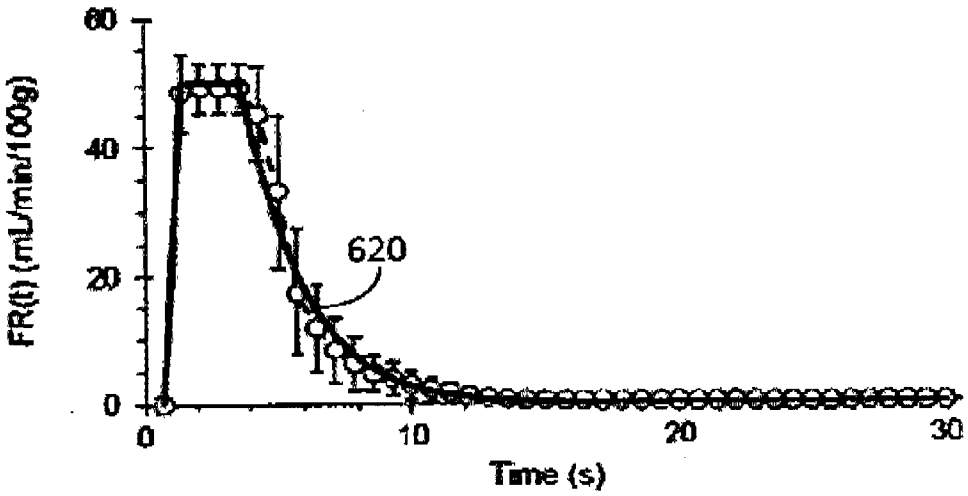

60
40
20
0
FR(t) (mL/min/100g)
620
0
10
20
30
Time (s)

FIG. 6B

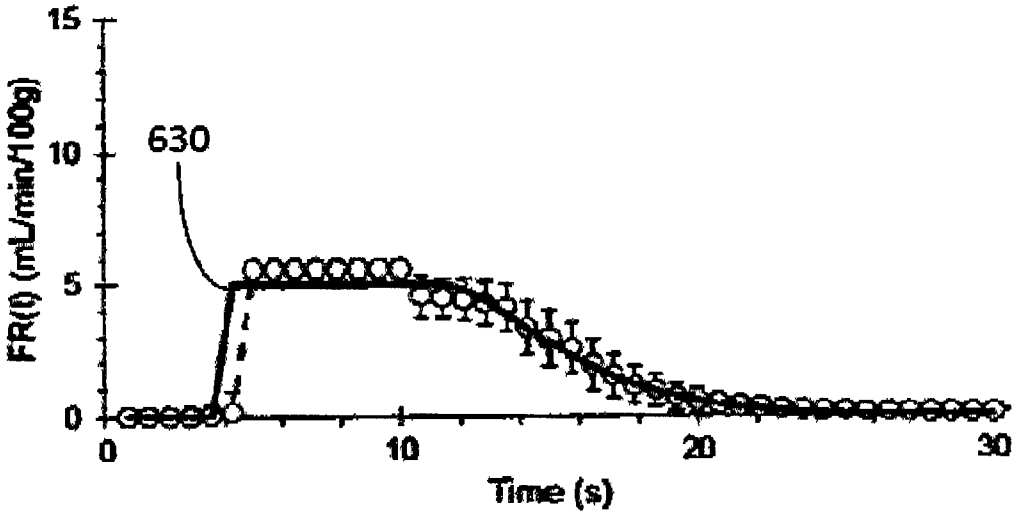

15
10
5
0
FR(t) (mL/min/100g)
630
0
10
20
30
Time (s)

FIG. 6C

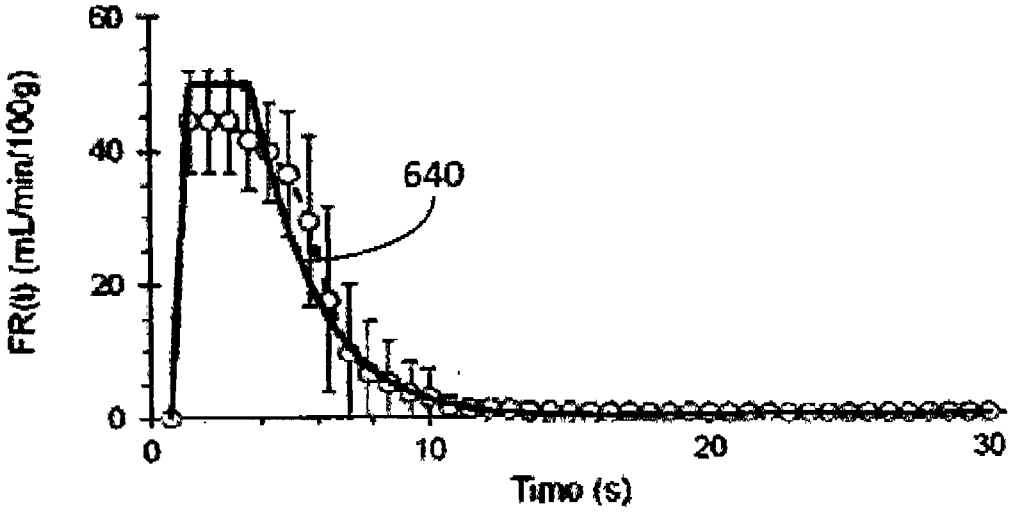

60
40
20
0
FR(t) (mL/min/100g)
640
0
10
20
30
Time (s)

FIG. 6D

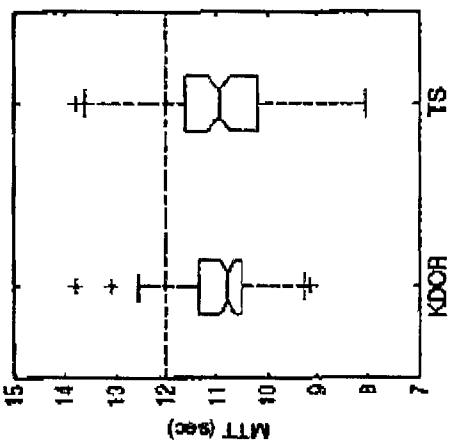


FIG. 7C

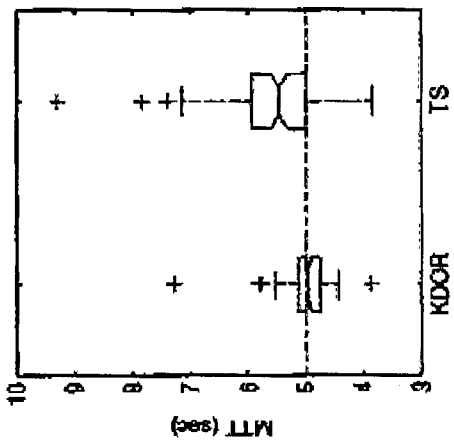


FIG. 7F

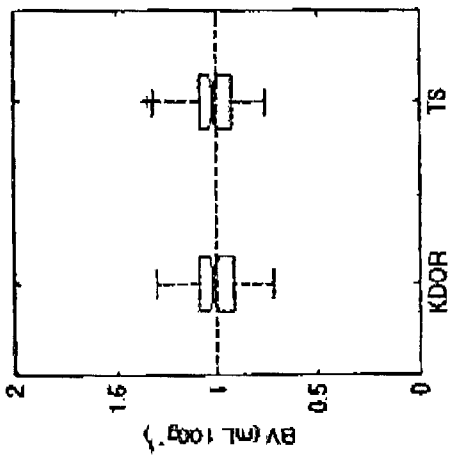


FIG. 7B

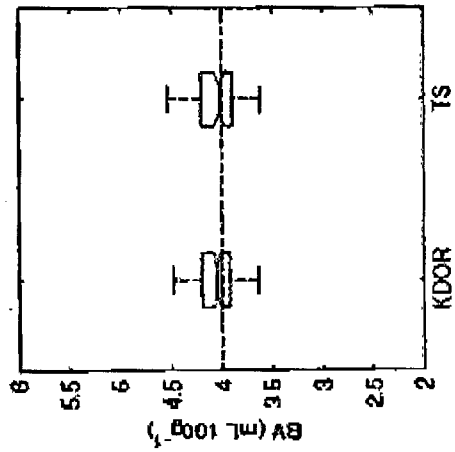


FIG. 7E

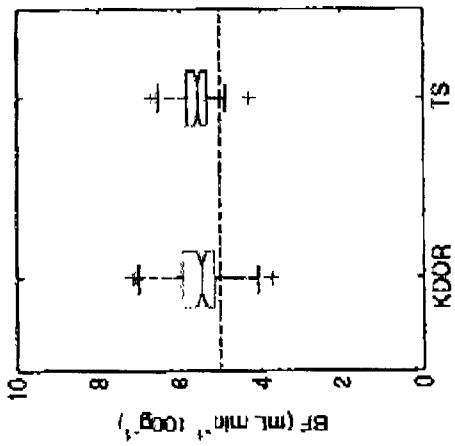


FIG. 7A

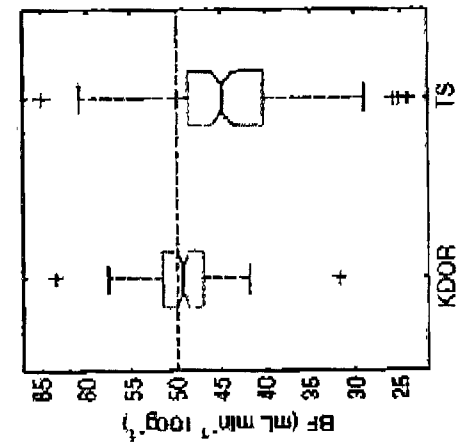


FIG. 7D

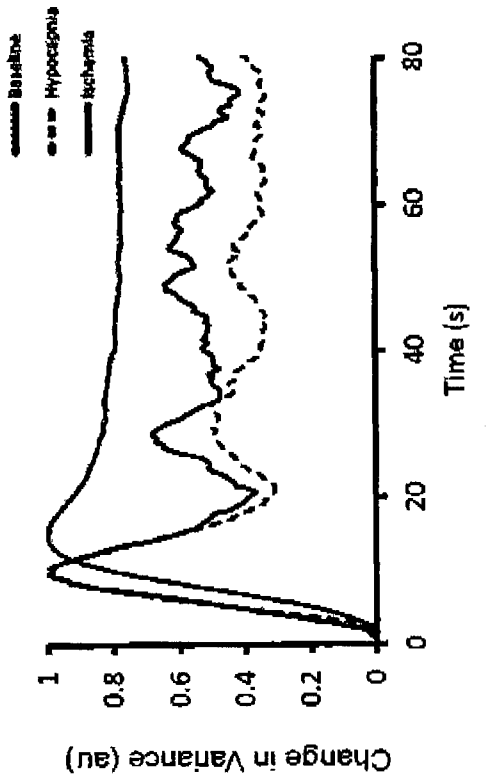

Baseline
Hypocapnia
Ischemia
Change in Variance (au)
1
0.8
0.6
0.4
0.2
0
0
20
40
60
80
Time (s)

FIG. 8B

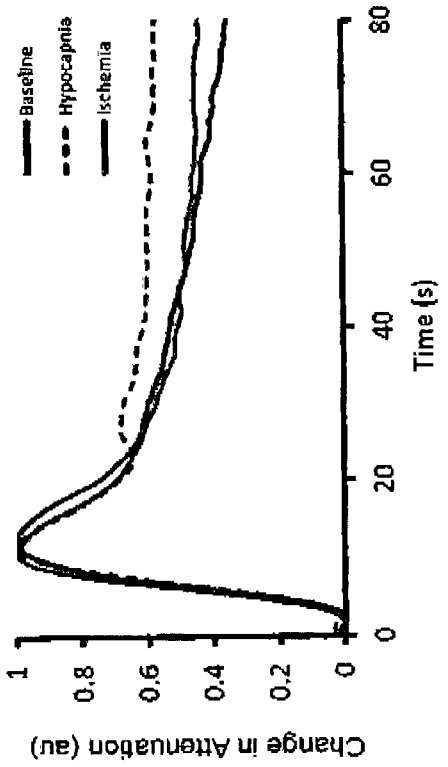

Baseline
Hypocapnia
Ischemia
Change in Attenuation (au)
1
0.8
0.6
0.4
0.2
0
0
20
40
60
80
Time (s)

FIG. 8A

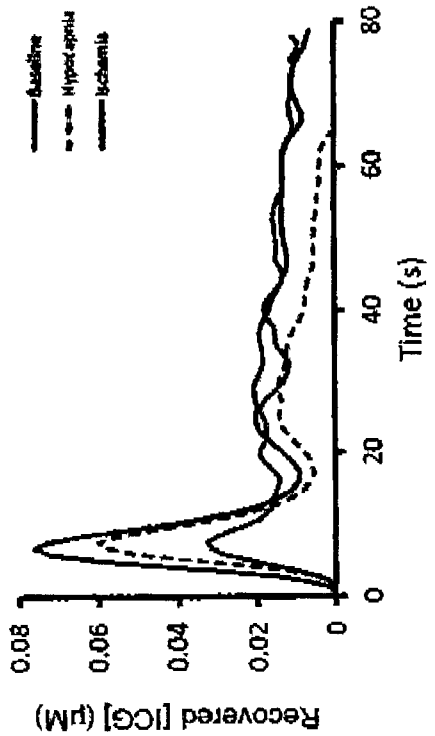

Baseline
Hypocapnia
Ischemia
Recovered [ICG] (μM)
0.08
0.06
0.04
0.02
0
0
20
40
60
80
Time (s)

FIG. 9B

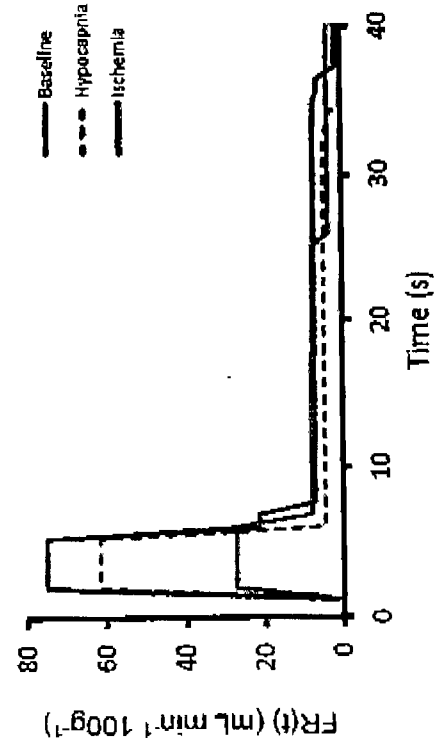

Baseline
Hypocapnia
Ischemia
FR(t) (mL min-1 100g-1)
80
60
40
20
0
0
10
20
30
40
Time (s)

FIG. 9A

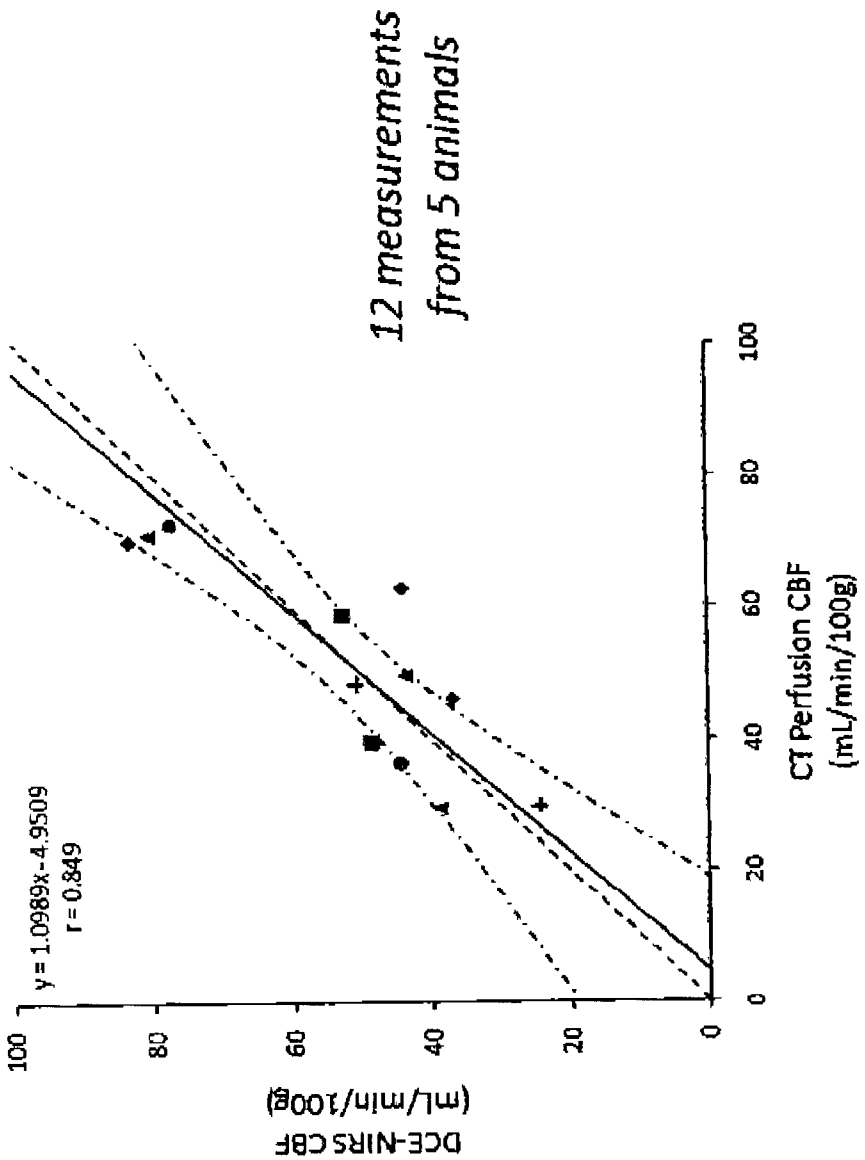

12 measurements
from 5 animals
y = 1.0989x-4.9509
r = 0.849
DCE-NIRS CBF
(mL/min/100g)
CT Perfusion CBF
(mL/min/100g)
0
20
40
60
80
100

FIG. 10

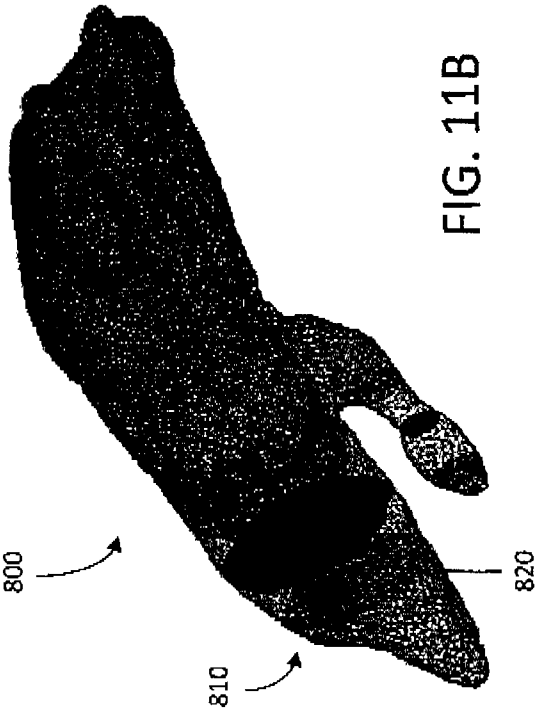


FIG. 11B

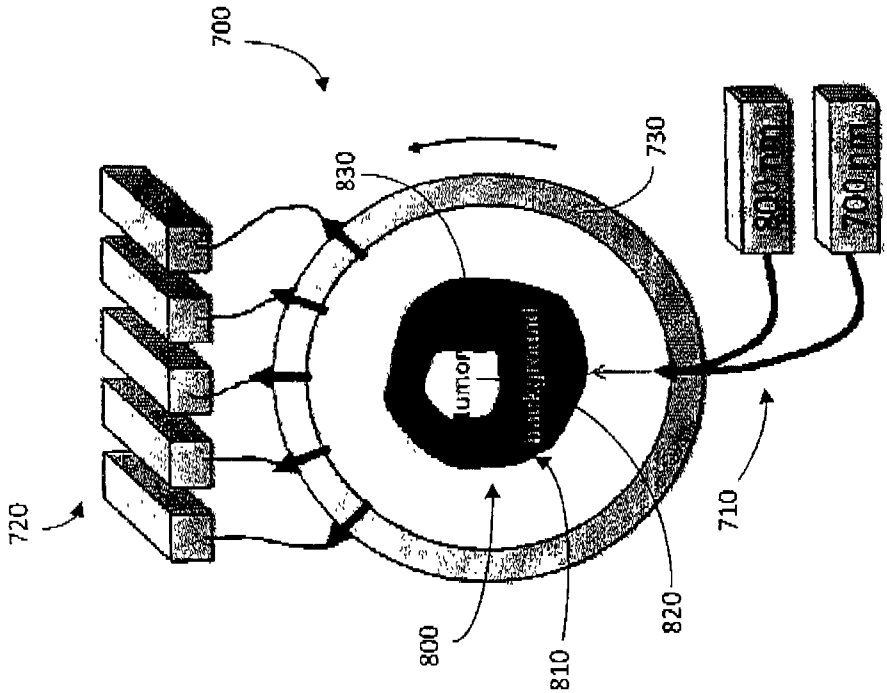


FIG. 11A

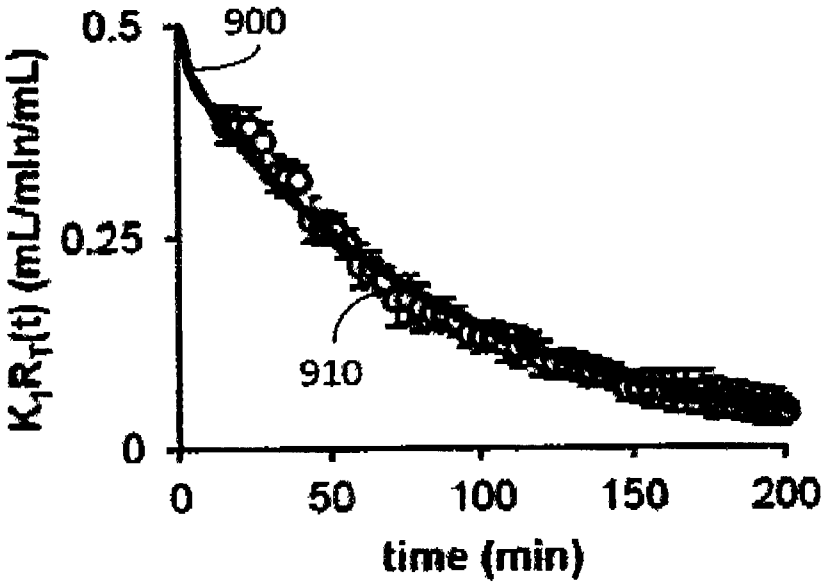


FIG. 12A

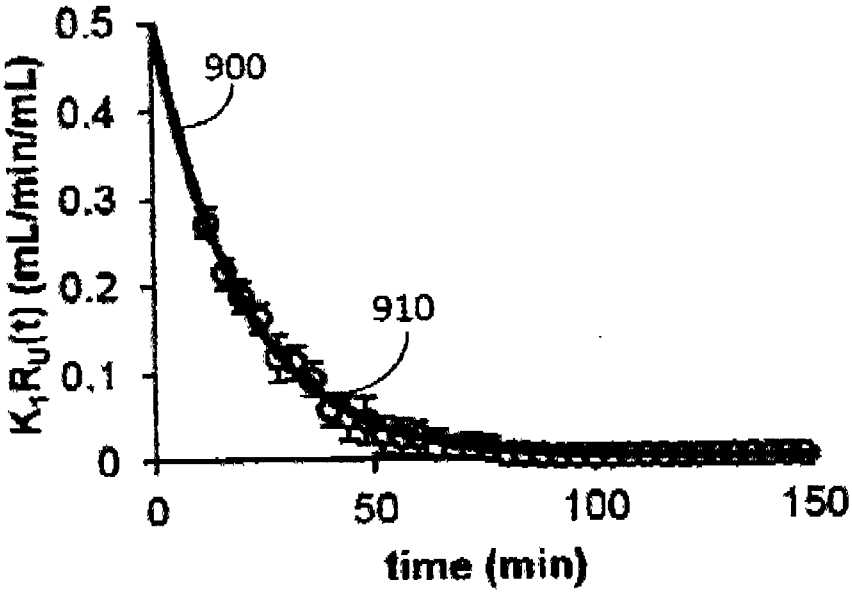


FIG. 12B

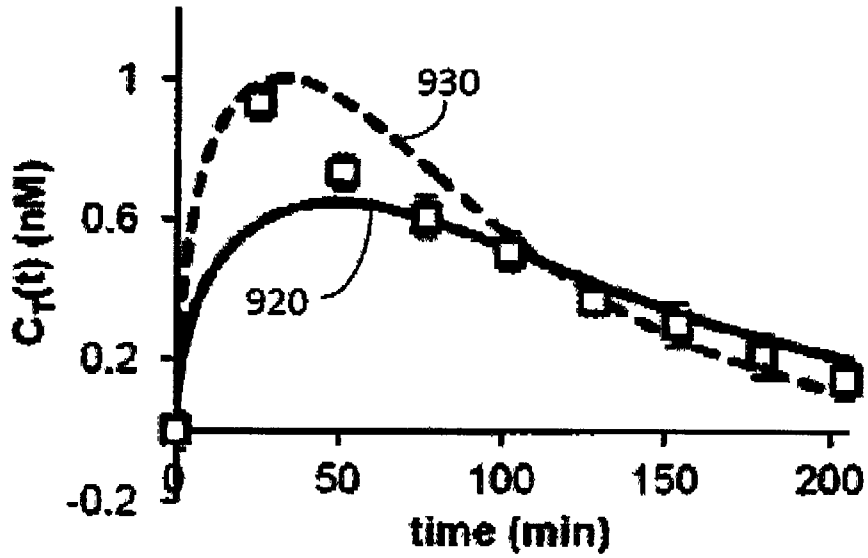


FIG. 12C

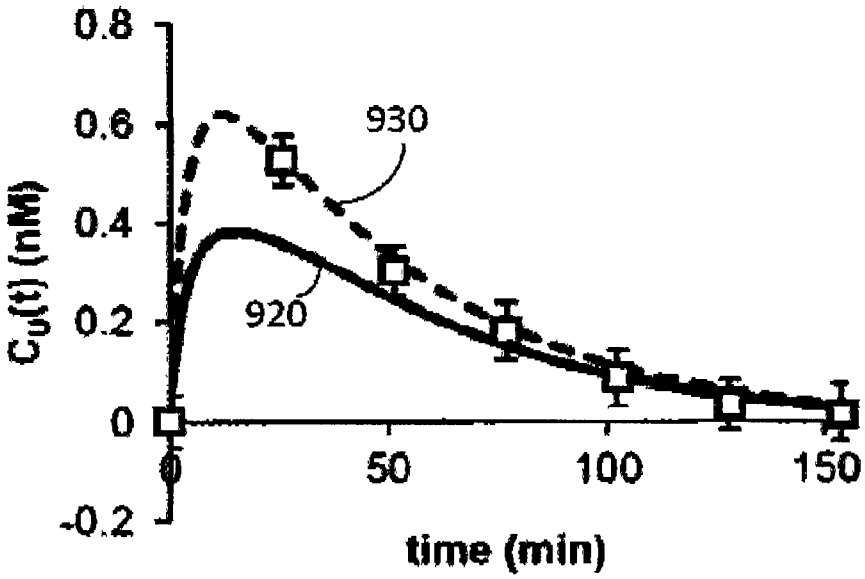


FIG. 12D

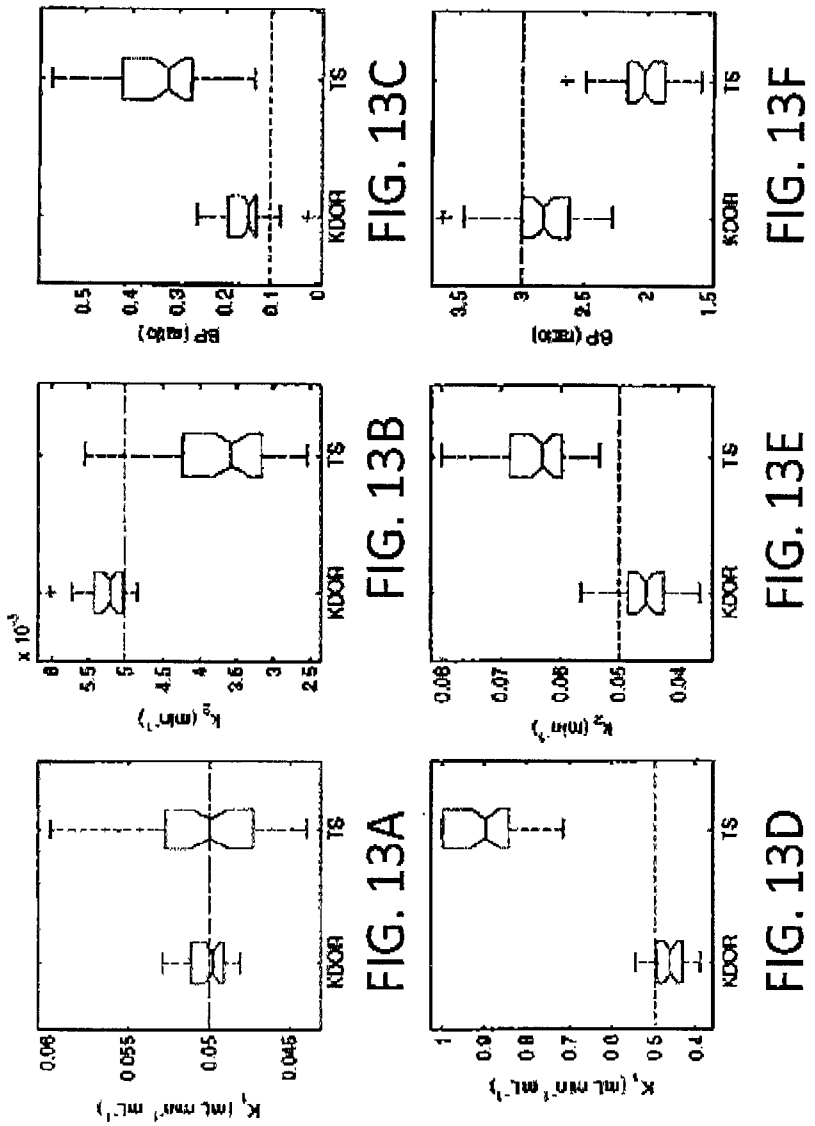


FIG. 13A FIG. 13B FIG. 13C FIG. 13D FIG. 13E FIG. 13F

INTERNATIONAL SEARCH REPORT

International application No.
PCT/CA2013/000202

A. CLASSIFICATION OF SUBJECT MATTER
IPC: ***A61B 6/00*** (2006.01) , ***A61B 5/026*** (2006.01) , ***A61B 5/0275*** (2006.01) , ***A61B 6/12*** (2006.01) , *G01T 1/164* (2006.01)
According to International Patent Classification (IPC) or to both national classification and IPC

B. FIELDS SEARCHED

Minimum documentation searched (classification system followed by classification symbols)
IPC (2006): G06F

Documentation searched other than minimum documentation to the extent that such documents are included in the fields searched

Electronic database(s) consulted during the international search (name of database(s) and, where practicable, search terms used)
Database: TotalPatent, Canadian Patent Database (Intellect), USPTO West, IEEE Xplore
Keywords: deconvolution, convolution, optical, reconstruction, dynamic contrast, constraint

C. DOCUMENTS CONSIDERED TO BE RELEVANT

Category*	Citation of document, with indication, where appropriate, of the relevant passages	Relevant to claim No.
X --- Y	Koh, T. S. et al., Assessment of Perfusion by Dynamic Contrast-Enhanced Imaging Using a Deconvolution Approach Based on Regression and Singular Value Decomposition, IEEE Transaction on Medical Imaging, volume 23, no. 12, pages 1532-1542, December 2004. * Abstract; page 1532, column 2, paragraph 1; page 1532, column 2, paragraph 2; page 1533, column 1, line 8 to column 2, line 29; pages 1534-1536, Section A page 1538, column 1, line 14 to column 2, line 20 *	1-6, 10-13, 17 and 18 --- 7-9, 14-16 and 19-21
Y	Pedersen, H. et al., A Unifying Model of Perfusion and Motion Applied to Reconstruction of Sparsely Sampled Free-Breathing Myocardial Perfusion MRI, Proceedings of IEEE International Symposium on Biomedical Imaging : From Nano to Macro, pages 752-755, 14-17 April 2010. * Pages 752-754, Section 2 *	7-9, 14-16 and 19-21
A	US 5994690 (KULKARNI et al.) 30 November 1999 (30-11-1999)	1-21
A	US 2011/0103542 (ALLMENDINGER et al.) 5 May 2011 (05-05-2011)	1-21

[X] Further documents are listed in the continuation of Box C. [X] See patent family annex.

* Special categories of cited documents :

"A" document defining the general state of the art which is not considered to be of particular relevance

"E" earlier application or patent but published on or after the international filing date

"L" document which may throw doubts on priority claim(s) or which is cited to establish the publication date of another citation or other special reason (as specified)

"O" document referring to an oral disclosure, use, exhibition or other means

"P" document published prior to the international filing date but later than the priority date claimed

"T" later document published after the international filing date or priority date and not in conflict with the application but cited to understand the principle or theory underlying the invention

"X" document of particular relevance; the claimed invention cannot be considered novel or cannot be considered to involve an inventive step when the document is taken alone

"Y" document of particular relevance; the claimed invention cannot be considered to involve an inventive step when the document is combined with one or more other such documents, such combination being obvious to a person skilled in the art

"&" document member of the same patent family

Date of the actual completion of the international search	Date of mailing of the international search report
28 June 2013 (28-06-2013)	15 July 2013 (15-07-2013)

Name and mailing address of the ISA/CA	Authorized officer
Canadian Intellectual Property Office Place du Portage I, C114 - 1st Floor, Box PCT 50 Victoria Street Gatineau, Quebec K1A 0C9 Facsimile No.: 001-819-953-2476	Alan Chan (819) 934-7888

INTERNATIONAL SEARCH REPORT

International application No.
PCT/CA2013/000202

C (Continuation). DOCUMENTS CONSIDERED TO BE RELEVANT

Category*	Citation of document, with indication, where appropriate, of the relevant passages	Relevant to claim No.
A	US 2003/0031299 (OHISHI) 13 February 2003 (13-02-2003)	1-21
A	US 2009/0185191 (BOPPART et al.) 23 July 2009 (23-07-2009)	1-21
A	US 6507633 (ELBAKRI et al.) 14 January 2003 (14-01-2003)	1-21

INTERNATIONAL SEARCH REPORT
Information on patent family members

International application No.
PCT/CA2013/000202

Patent Document Cited in Search Report	Publication Date	Patent Family Member(s)	Publication Date
US5994690A	30 November 1999 (30-11-1999)	None	
US2011103542A1	05 May 2011 (05-05-2011)	CN102048552A	11 May 2011 (11-05-2011)
		DE102009051384A1	12 May 2011 (12-05-2011)
		US8279996B2	02 October 2012 (02-10-2012)
US2003031299A1	13 February 2003 (13-02-2003)	DE60205682D1	29 September 2005 (29-09-2005)
		DE60205682T2	14 June 2006 (14-06-2006)
		EP1271408A2	02 January 2003 (02-01-2003)
		EP1271408A3	10 December 2003 (10-12-2003)
		EP1271408B1	24 August 2005 (24-08-2005)
		JP2003000580A	07 January 2003 (07-01-2003)
		JP4854137B2	18 January 2012 (18-01-2012)
		US6845142B2	18 January 2005 (18-01-2005)
US2009185191A1	23 July 2009 (23-07-2009)	US2009185191A1	23 July 2009 (23-07-2009)
		US8115934B2	14 February 2012 (14-02-2012)
US6507633B1	14 January 2003 (14-01-2003)	None	